submitted to *Geophys. J. Int.*

Transdimensional Love-wave tomography of the British Isles and shear-velocity structure of the East Irish Sea Basin from ambient-noise interferometry

Erica Galetti,[1] Andrew Curtis,[1] Brian Baptie,[2] David Jenkins,[1,3] Heather Nicolson[1,2,4]

[1] *University of Edinburgh, School of GeoSciences, James Hutton Road, Edinburgh EH9 3FE, United Kingdom*

[2] *British Geological Survey, Murchison House, West Mains Road, Edinburgh EH9 3LA, United Kingdom*

[3] *Now at WesternGeco Ltd, Schlumberger House, Buckingham Gate, Gatwick Airport, West Sussex, RH6 0NZ, United K*

[4] *Now at Wood Mackenzie, Exchange Place 2, 5 Semple Street, Edinburgh EH3 8BL, United Kingdom*

SUMMARY

We present the first Love-wave group velocity and shear velocity maps of the British Isles obtained from ambient noise interferometry and fully non-linear inversion. We computed interferometric inter-station Green's functions by cross-correlating the transverse component of ambient noise records retrieved by 61 seismic stations across the UK and Ireland. Group velocity measurements along each possible inter-station path were obtained using frequency-time analysis and converted into a series of inter-station traveltime datasets between 4 and 15 seconds period. Traveltime uncertainties estimated from the standard deviation of dispersion curves constructed by stacking randomly-selected subsets of daily cross-correlations, were observed to be too low to allow reasonable data fits to be obtained during tomography. Data uncertainties were therefore estimated again during the inversion as distance-dependent functionals. We produced Love-wave group velocity maps within 8 different period bands using a fully non-linear tomography method which combines the transdimensional reversible-jump Markov chain Monte Carlo (rj-McMC) algorithm with an

eikonal raytracer. By modelling exact raypaths at each step of the Markov chain we ensured that the non-linear character of the inverse problem was fully and correctly accounted for. Between 4 and 10 seconds period, the group velocity maps show remarkable agreement with the known geology of the British Isles and correctly identify a number of low-velocity sedimentary basins and high-velocity features. Longer period maps, in which most sedimentary basins are not visible, are instead mainly representative of basement rocks. In a second stage of our study we used the results of tomography to produce a series of Love-wave group velocity dispersion curves across a grid of geographical points focussed around the East Irish Sea sedimentary basin. We then independently inverted each curve using a similar rj-McMC algorithm to obtain a series of one-dimensional shear velocity profiles. By merging all 1D profiles, we created a fully three-dimensional model of the crust beneath the East Irish Sea. The depth to basement in this model compares well with that averaged from seismic reflection profiles. This result is the first 3-dimensional model in the UK with fully quantified uncertainties: it shows basin depths and basement structures, and their concomitant uncertainties.

Key words: seismic interferometry – ambient noise – tomography – Love waves – reversible-jump algorithm – Markov chain Monte Carlo – surface wave dispersion – shear velocity – British Isles – Irish Sea

1 INTRODUCTION

Over the last ten years, seismic interferometry has revolutionised the way seismologists study the Earth's interior by providing novel ways to obtain information about the subsurface from naturally-occurring seismic ambient noise. Seismologists extract such information by cross-correlating noise recordings at pairs of seismic receivers. So doing yields an estimate of the Green's function between the two receiver locations (Campillo & Paul 2003; Wapenaar 2004; Snieder 2004; van Manen et al. 2005, 2006; Wapenaar & Fokkema 2006). Since most ambient-noise sources are located near the surface of the Earth, Green's function estimates from noise cross-correlations typically contain mainly the surface-wave component of the wavefield that would have propagated between the two receivers if one of them had in fact been a source

(a so-called virtual source). These Green's function estimates in turn constrain the range of possible subsurface structures. Reviews of interferometric methods are given in Curtis et al. (2006), Schuster (2009), Wapenaar et al. (2010a), Wapenaar et al. (2010b) and Galetti & Curtis (2012).

Within the context of seismic tomography and imaging, seismic interferometry has significantly enhanced our ability to image the Earth's interior. Particularly, since the natural distribution of earthquakes is strongly irregular and mainly localised to plate margins, interferometry provides a powerful tool for crustal seismologists by allowing virtual sources to be placed even in seismically quiescent regions. In addition, since inter-receiver paths are usually shorter than teleseismic ones, attenuation effects at low periods are generally lower, making the signal-to-noise ratio substantially higher. The resulting method of *ambient-noise tomography* (ANT) makes use of information retrieved from ambient-noise cross-correlations, rather than earthquake records, to invert for subsurface structure. First applied to observational data by Shapiro et al. (2005) and Sabra et al. (2005), ANT has been used at regional and continental scales to produce group-velocity maps using mainly Rayleigh-wave cross-correlations, but a number of studies have also used Love-wave cross-correlations to image Europe (Li et al. 2010a), Asia (Cho et al. 2007; Li et al. 2010b), North America (Bensen et al. 2008; Lin et al. 2008; Roux 2009), and Australia (Saygin & Kennett 2010). In addition, ANT has been used successfully to produce images of smaller-scale structures such as volcanic edifices (Masterlark et al. 2010; Jay et al. 2012; Nagaoka et al. 2012) and inhomogeneities in oil and gas fields (Haney & Douma 2010, 2012), as well as of local structures at engineering seismology scales (Picozzi et al. 2009; Pilz et al. 2012) and on the seabed (de Ridder & Dellinger 2011; Mordret et al. 2013a,b; de Ridder et al. 2014).

Just as the natural distribution of earthquakes is strongly irregular, the distribution of seismic stations over the Earth's surface is far from uniform with many areas (e.g., central Africa, Russia, northern Canada) having very little coverage. Certain regions such as the USA are well covered by dense receiver networks, and others (e.g., Australia and South America) have variable coverage with higher station density in areas of higher seismic activity or population. Due to irregularities in the distribution of seismic receivers, the resolution achievable with ANT may vary greatly across regions which are unevenly sampled, being higher in areas that are more densely covered by receivers and decreasing where station density is low. Choosing an appropriate inversion method to perform ANT that correctly compensates for variable station coverage is therefore particularly important.

A variety of tomographic methods that take non-uniform sampling into account have been

developed using irregular model parametrisations, and an extensive overview of these methods can be found in Rawlinson et al. (2010). Recently, an implementation of model parametrisation that uses Voronoi cells was proposed by Bodin & Sambridge (2009), who used Bayes' theorem, Markov-Chain Monte Carlo (McMC) and the reversible-jump algorithm to invert traveltime data over a large number of velocity models and obtain an ensemble of solutions which are distributed according to the posterior probability density function (PDF). This method is referred to as 'transdimensional', in the sense that the number of parameters is itself one of the quantities which are free to vary during inversion. Hence, the method can be mainly data driven as it requires only minimal assumptions to be made within prior probability distributions on the various parameters. When little information on the model is available before the inversion, prior distributions may be set to uninformative uniform distributions with wide bounds, ensuring that the final models are not biased by the choice of the prior. Compared to more traditional inversion methods that keep the model parametrisation fixed, this method is particularly flexible as it dynamically adapts to non-uniform data coverage without requiring the use of any arbitrary regularisation (e.g., damping or smoothing), and was used successfully by Bodin & Sambridge (2009) to obtain Rayleigh-wave velocity models of Australia from ambient-noise interferometry. While Young et al. (2013) applied the method to image the Tasmanian crust, Galetti et al. (2015) further generalised the method by making it fully non-linear: they showed that if both model parametrisation and raypaths are allowed to vary freely simultaneously, then the method also defines loop-like uncertainty structures around isolated low- and high-velocity anomalies which define the spatial resolution of those structures.

Within this study, we first use the horizontal components of seismic ambient noise recorded by UK seismic stations to produce a set of inter-station Green's functions. From these interferometric Green's functions we determine Love-wave traveltimes between all possible station pairs, and use this set of traveltimes to perform Love-wave tomography of the British Isles. This region has a low level of earthquake activity (Baptie 2010) and could not easily be imaged using surface waves and local-earthquake tomography methods. In fact, although the UK's upper mantle and Scotland's crust have been imaged using body waves (Arrowsmith et al. 2005; Luckett & Baptie 2015), the UK-wide crust has not been imaged as a whole, in part because local earthquakes are seldom sufficiently large to generate clear surface wave arrivals. Our study follows from Nicolson et al. (2012, 2014), who applied seismic interferometry to vertical-component ambient-noise records from the UK and used the reconstructed Green's functions to produce Rayleigh-wave group-velocity maps of the British Isles using

the linearised inversion method of Rawlinson & Sambridge (2005). Here we extend the analysis of Nicolson et al. (2012, 2014) to the horizontal components of ambient-noise recorded by several seismic networks deployed at different times. Because these networks have significantly different spatial extents, we employed a fully non-linear inversion method (such as in Galetti et al. (2015)) which combines the linearised rj-MCMC algorithm of Bodin & Sambridge (2009) with an eikonal raytracer (Rawlinson & Sambridge 2004, 2005) to update the raypath geometry at each step of the Markov chain. Compared to the linearised fast-marching tomography method used by Nicolson et al. (2012, 2014), the choice of rj-McMC tomography ensured that the datasets obtained from the different networks were correctly integrated with variable parametrisation as required by the data density, and indeed that the uncertainty in the derived travel time data can be treated as a parametrised unknown and estimated during the inversion. Compared to the partially linearised rj-McMC method of Bodin & Sambridge (2009) and Young et al. (2013), Galetti et al. (2015) show that tomographic uncertainties are better estimated by this fully non-linearised method.

In this paper, we first describe of the geological setting and seismicity of the British Isles. We then outline the data processing flow and the fully non-linear inversion method which we implemented to perform the inversions, present Love-wave group-velocity maps at various periods, and discuss their significance. Finally, we use Love-wave group velocities retrieved from the tomographic maps to produce a 3D shear-velocity model of the East Irish Sea sedimentary basin and show that it compares well to other independent information about the basin; however, whereas similar independent information is only available for certain areas, the Love-wave information is available across the entire mainland UK.

2 GEOLOGICAL SETTING AND SEISMICITY OF THE BRITISH ISLES

The British Isles are an intra-plate archipelago located in the north-west of the European shelf at the north-east margin of the Atlantic Ocean. The current geology of the British Isles is the result of a complex structural and tectonic history combining several deformation events with under-plating and isostatic uplift.

The basement of the British Isles is composed of a complex amalgamation of discrete terranes (fault-bounded blocks with a distinct geological history) of Precambrian and Lower Palaeozoic age (Fig. 1). Plate motion reconstructions show that in the Lower Palaeozoic the northern part of the British Isles (Scotland and north-west Ireland) was located on the accretionary margin of Laurentia, while the southern part (England, Wales, south-east Ireland) was located on the active margin of the Avalonian micro-continent. The terranes were joined

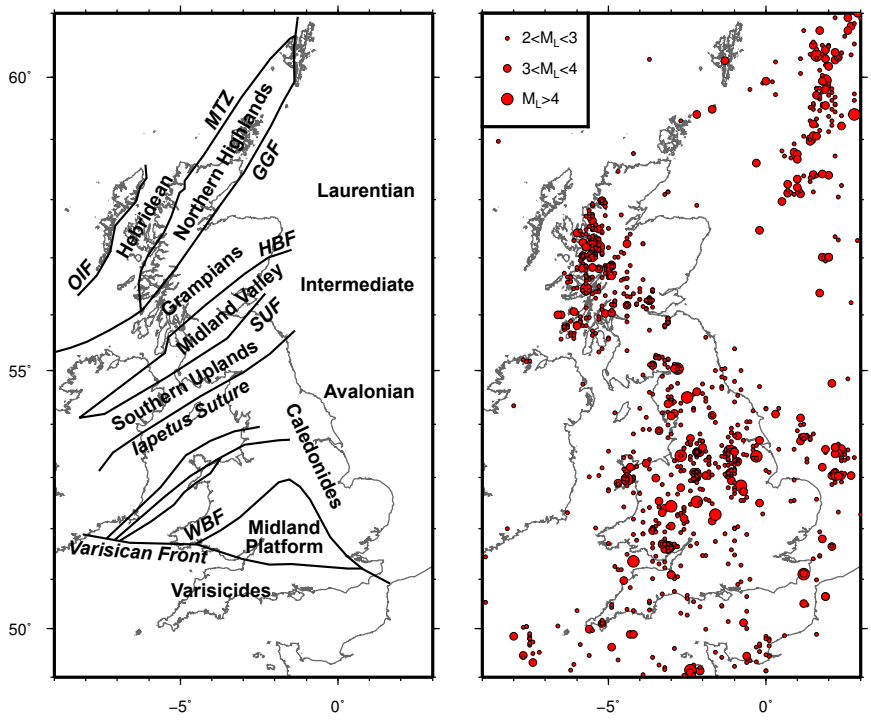

Figure 1. Terrane boundaries (left) and seismicity (right) in the British Isles. The boundaries between the different geological terranes are after Woodcock & Strachan (2012) and are abbreviated as follows: Outer Isles Thrust (OIT); Moine Thrust (MTZ); Great Glen Fault (GGF); Highland Boundary Fault (HBF); Southern Uplands Fault (SUF); Welsh Borderland Fault System (WBF). The circles in the right-hand map denote the location of earthquakes with $M_L \geq 2$ occurred between 1970 and 2014 as reported in the British Geological Survey catalogue (British Geological Survey 2015), with the size of the circles denoting earthquake Richter magnitude.

together during the Caledonian orogeny, which occurred across the Ordovician, Silurian and Devonian periods (∼480–380 Ma) and caused the closure of the Iapetus Ocean as Laurentia and Avalonia collided. The closure of the Iapetus Ocean is currently marked by the Iapetus Suture, which runs from north-east England (almost along the current border between Scotland and England), across the East Irish Sea and towards south-west Ireland.

Prior to the Caledonian orogeny, the Laurentian and Avalonian blocks underwent very different geological histories which resulted in the formation of very distinct lithological bodies in the two regions. The Laurentian part is characterised by the presence of high-grade metamorphic (Lewisian gneisses) and meta-sedimentary (Moine and Dalradian supergroups) complexes north of the Highland Boundary Fault, island-arc volcanics and aeolian sediments in the Midland Valley, and sandstones and mudstones in the Southern Uplands. The Avalonian part includes island-arc volcanics, resulting from its location next to the passive destructive

margin of Gondwana in the Neoproterozoic, and granitic plutons and deformed volcanic-sedimentary sequences from the Cadomian orogeny in the late Neoproterozoic (650–550 Ma). However, most of the pre-Caledonian evidence of Avalonia is now covered by the products of the Varisican orogeny (Devonian and Carboniferous periods), which occurred as the Armorican micro-continent collided with Avalonia as the plate motion that had previously caused the Caledonian orogeny continued. Evidence of the Varisican orogeny can be found in the Varisicides in the south of England, bounded to the north by the Varisican Front which separates them from the more weakly deformed rocks to the north. A large granitic batholith was emplaced in Devon and Cornwall towards the end of the Varisican orogeny, and the Rheic Ocean eventually closed as the continent collided with Gondwana, forming the supercontinent Pangaea and bringing the components of the British Isles to their approximately present position by the early Permian.

In terms of seismicity, the British Isles are characterised by low levels of earthquake activity, as earthquakes tend to be infrequent and of relatively small magnitude. For instance, estimates of activity rates suggest that a moment magnitude (M_W) 5.0 earthquake is likely to occur in the British Isles every 50 years, and the largest observed earthquake to-date had a magnitude of of 5.9 M_W. Figure 1 shows seismicity in the British Isles between 1970 and 2014. The distribution of earthquake epicentres in the British Isles is heterogeneous, with almost no seismic activity in the north-east of mainland Britain, Ireland and the north-west Atlantic margin. Most earthquakes are located along a north-south band which mainly spans the western flank of mainland Britain. This band is relatively narrow in Scotland and increases in width towards the south.

The biased distribution of earthquakes, the absence of large-magnitude events, and the fact that many historical earthquakes were not recorded on digital seismometers, impose a limit on our ability to image the region tomographically using local active sources. Seismic tomography using teleseismic earthquakes also presents a number of challenges due to large attenuation at low periods and to the fact that information in their seismograms is not limited to the British Isles geographical area (i.e., it is confounded with information about Earth properties along the rest of the teleseismic paths of energy propagation). In addition, the irregular geometry of the stations used in this study (Fig. 2) precludes the use of tomography methods that benefit from the availability of dense or regular arrays of stations (e.g., Helmholtz tomography Lin & Ritzwoller (2011)). In fact, only a limited number studies have so far attempted to image the crust and upper mantle beneath the British Isles using traditional earthquake tomography methods (Arrowsmith et al. 2005; Luckett & Baptie 2015). However, being an archipelago

bounded by the Atlantic Ocean to the west, the North Sea to the east and the Norwegian Sea to the north, the British Isles are naturally surrounded by sources of seismic ambient noise, including the primary (12–14 seconds period) and secondary (6–8 seconds period) oceanic microseisms, waves, wind and ocean currents. Since these sources are relatively constant and repeatable, the British Isles are therefore an ideal region for a tomographic study which uses ambient-noise interferometry.

3 DATA AND PROCESSING

3.1 Station networks

Ambient noise was recorded by a number of seismic networks that were deployed across the British Isles at different times (Fig. 2). The Reflections Under the Scottish Highlands (RUSH-II) network is a temporary array of twenty-four broadband seismometers (of which only twenty-three were used in this study) that were active between 2001 and 2003. Because the main purpose of the RUSH-II array was to record reflections in order to identify mantle reflectors beneath Scotland (Asencio et al. 2003; Bastow et al. 2007), the network was arranged along three approximately linear profiles with an average station separation of about 15 km, which is ideal for reflection studies but not for tomography. The main UK-wide deployment of seismic stations (which also includes one station in Ireland) is an ensemble of thirty-nine broadband stations, mainly located in southern England, which belong to different networks: British Geological Survey (BGS), GEOFON, Atomic Weapons Establishment (AWE) Blacknest, and British Isles Seismic Experiment (BISE). Continuous noise records were obtained for most of 2010 at BGS, GEOFON and AWE Blacknest stations, and for 2006-2007 at BISE stations, which were included in the dataset in an attempt to improve the resolution in the east-west direction. As some of the BGS, GEOFON and AWE Blacknest stations were also active during the recording period of BISE, inter-network noise cross-correlations with BISE stations could be calculated in some cases. However, since none of the RUSH-II stations were recording at time periods in common with any of the other available networks, the datasets obtained from the RUSH-II project and from the UK-wide array can be considered completely separate and independent as no inter-network cross-correlations could be calculated.

3.2 Data processing

All networks recorded the vertical (Z) and the two horizontal (north, N, and east, E) components of ground motion, and thanks to the proximity to the Atlantic Ocean the recorded data

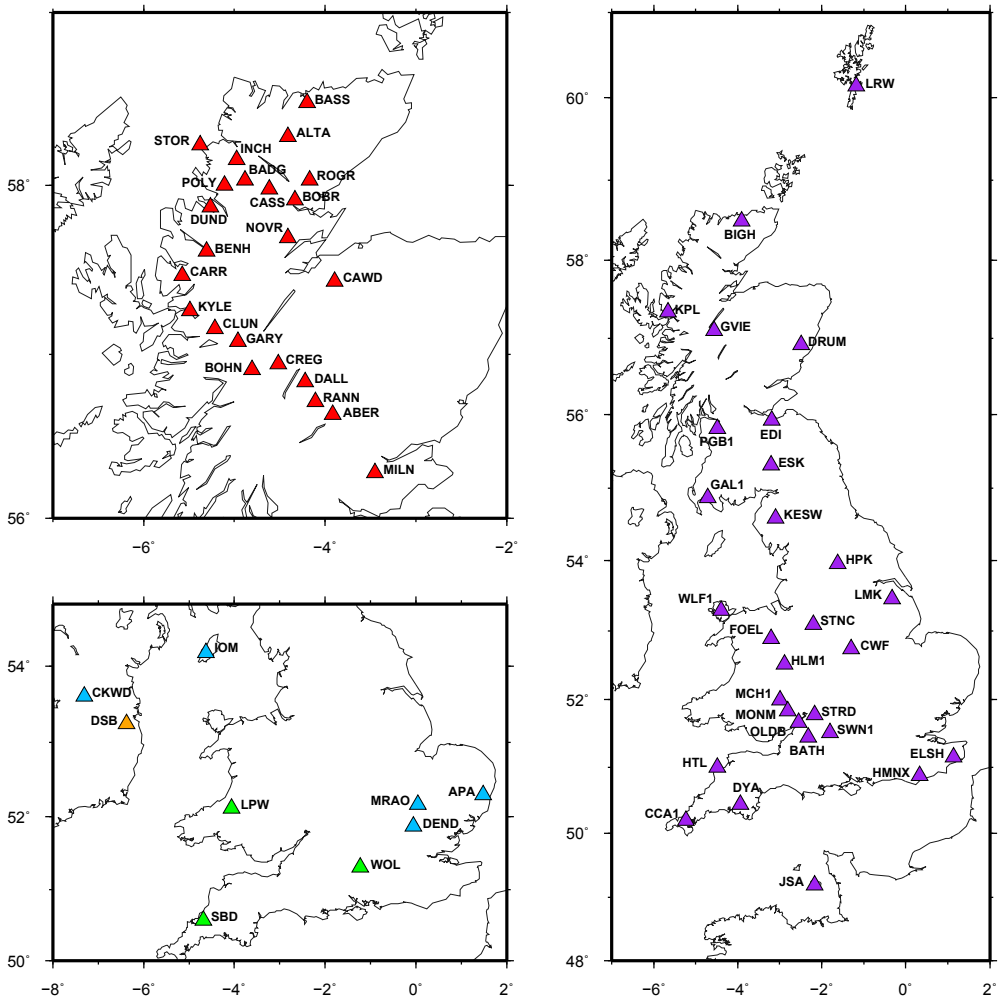

Figure 2. Location map of RUSH-II (red triangles), BGS (purple triangles), AWE Blacknest (green triangles), BISE (blue triangles) and GEOFON (orange triangles) stations.

were characterised by a strong component of oceanic microseismic noise, which contributed to a great extent to the reconstruction of the inter-receiver Green's functions.

In order to obtain meaningful travel time measurements that could be used to perform tomography from ambient noise, we approximately followed the method outlined by Bensen et al. (2007) to process the data. The noise records were first divided into 24-hour-long files and then decimated to one sample per second after applying an anti-aliasing filter. The mean and trend were also removed from each day-file together with the instrumental response.

Compared to the data processing workflow normally applied to the vertical component of ground motion (Bensen et al. 2007), the processing of horizontal components required a number of additional steps prior to cross-correlation. In order to compute Love waves from horizontal component data, the N and E components were rotated into the transverse and

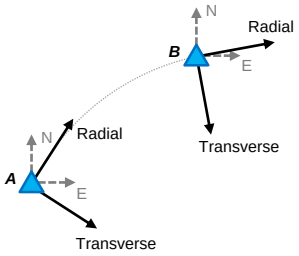

Figure 3. Definition of radial and transverse components of ground motion with respect to the recorded north (N) and east (E) components. The dashed grey line joining the two triangles represents the great circle arc connecting stations A and B.

radial directions. These directions can be computed for each receiver pair by defining a great circle path joining the two receivers, as shown in Fig. 3: supposing inter-receiver interferometry turns station A into a virtual source whose signal is recorded at station B, the horizontal components of ground motion have to be rotated such that the radial component lies along the great circle path joining the two stations and points from virtual source A to receiver B, and the transverse component lies ninety degrees with respect to the radial direction.

The effects of large amplitude events such as earthquakes were removed by normalising the transverse components in the time domain using one-bit normalisation, and the normalised day-files were then spectrally whitened in order to reduce the effect of monochromatic noise sources and to broaden the frequency spectrum of the data. As temporal and spectral normalisation introduce non-linear changes into the data, it was necessary for these steps to be applied after rotation into the transverse and radial directions.

Cross-correlations of transverse day-files were then computed for all possible station pairs and linearly stacked over the total recording period in order to increase the signal-to-noise ratio. While other forms of stacking have been proposed more recently such as phase-weighted stacking (Schimmel & Paulssen 1997; Schimmel et al. 2011), we have performed extensive tests with these methods on inter-station Green's functions computed across the UK landmass or on paths crossing the North Sea (using stations in surrounding countries), and found that they can be problematic when the frequency spectrum is not completely uniform. We therefore apply only the above stacking to be consistent with the previous UK studies of Nicolson et al. (2012) and Nicolson et al. (2014).

Since a measurement should be repeatable in time to be considered valid, we initially followed the approach of Lin et al. (2007) to estimate traveltime uncertainties by producing additional subsets of cross-correlation stacks: each stack contained an equal number of randomly-selected daily cross-correlations, with each day being present in only one indepen-

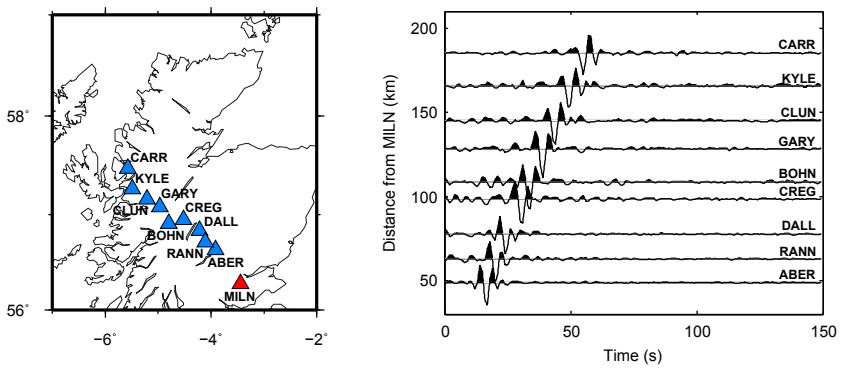

Figure 4. Example of Green's function emergence along an array of stations in the Scottish Highlands. Station MILN (red triangle) acts as a virtual source whose signal is recorded by the array of stations indicated by the blue triangles.

dent random stack. The uncertainty in the estimated Green's functions for each receiver pair was reflected in its variability across the independent random stacks.

The result of cross-correlation of seismic signals is a trace which is twice the length of the original ones, with a positive (causal) and a negative (acausal) part representing seismic energy travelling in opposite directions between the two receivers. If noise sources were uniformly distributed in space, the causal and acausal components would be perfectly symmetric around zero lag time. In reality, noise sources are not uniformly distributed around the British Isles, with the Atlantic Ocean providing most of the seismic energy and causing ambient noise to propagate mainly from west to east. However, both our data and previous studies (Nicolson et al. 2012, 2014) showed that this is not always the case, and different trends were found along different inter-station paths. Hence, since it was not possible to establish categorically whether the causal or acausal component was more reliable, we assumed both components to be equally valid and constructed the final, one-sided Green's functions by stacking the causal and time-reversed acausal parts. So doing allowed the data processing stage to be automated, but we are aware that it may have added the potential for some information to be lost along some paths due to the addition of components containing unreliable information. An example of the resulting one-sided Green's functions is shown in Fig. 4, where station MILN (red triangle) acts as a virtual source whose signal is recorded at a number of other stations (blue triangles). The surface wave move-out is clearly visible as the distance from MILN increases.

In order to test the validity of the interferometric Green's function computed between a pair of seismic stations, we can compare the results of interferometry with true earthquake recordings provided an earthquake occurred near the location of one of the stations. Figure 5 shows such comparison for the Folkstone earthquake, a 4.2-magnitude earthquake which

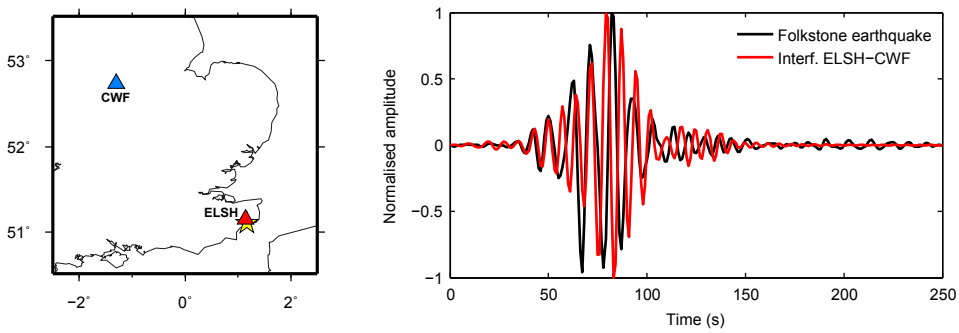

Figure 5. Comparison of the true recording of the Folkstone earthquake at station CWD (black solid line) and the interferometric trace constructed by cross-correlating ambient noise data recorded at stations ELSH and CWD (red solid line). Each trace is filtered between 3.8 and 6.2 s period, and normalised to its maximum amplitude. The earthquake epicentre is denoted by a yellow star in the map on the left.

occurred on 28 April 2007 at 07:18 UTC and was recorded by a number of seismic stations in the south of England. Although differences between the true and interferometric result are expected, the true trace (black solid line in Fig. 5) looks remarkably similar to the interferometric result obtained from ambient-noise interferometry between stations ELSH and CWF (red solid line in Fig. 5). The differences between the two traces can be explained by the presence of different effective source time-functions in the earthquake and noise records, and to the earthquake epicentre and station ELSH not being exactly co-located.

Rayleigh and Love surface waves are dispersive: within a surface-wave packet, longer-period waves penetrate deeper within the Earth due to their longer wavelength, while shorter-period waves mainly propagate in shallower layers. Because seismic velocity generally increases with depth, longer-period waves tend to travel faster than shorter-period ones, hence surface-wave arrivals of increasing period can be observed on a seismogram at progressively earlier times. Therefore, by analysing the traveltimes of surface waves at different periods we can obtain information on the Earth's structure at various depths. Similarly, the different types of particle motion that characterize surface Rayleigh and Love waves account for the different sensitivity of the two surface-wave types, with Love waves having higher sensitivity in shallower layers than Rayleigh waves (e.g., Curtis et al. (1998)). Hence, while Rayleigh-wave tomography can show geological structures down to the lower crust and upper mantle, Love-wave group velocity maps are expected to be more representative of shallow sedimentary and superficial layers. Within this study, we focused on the fundamental Love-wave mode and used the multiple-filter analysis method of Herrmann & Ammon (2002) to estimate arrival times and hence path-averaged group velocities at various periods for all available inter-station paths.

When multiple surface wave modes are present, the quality of interferometric Green's function estimates may be affected by the distribution of the ambient noise sources. For instance, Halliday & Curtis (2008) find that if noise sources are only located on the Earth's surface rather than also in the subsurface, interferometric Green's functions might be contaminated by spurious arrivals arising from the cross-correlation of different higher-mode surface waves. In addition, if the dispersion curves of fundamental and higher modes are similar, then higher modes might erroneously be interpreted as fundamental if their amplitude dominates or significantly affects the group energy arrival (Poli et al. 2013). For the purpose of this study, we ignored these two effects, assumed that the measured arrival times correctly estimated the arrival of the fundamental-mode Love waves, and instead attempted to quantify the uncertainty in these estimates.

We measured Love-wave dispersion on both the full and the randomly-stacked Green's functions, and initially estimated the uncertainty in group velocity at each period from the standard deviation of the group velocities of the independent random stacks. As suggested by Bensen et al. (2007), group velocity measurements between stations that were less than 3 wavelengths apart were considered unreliable and automatically rejected. Traveltime uncertainties from the randomly-stacked cross-correlations were also used as a means for quality control, as all paths with uncertainty greater than 5% of the total traveltime were excluded from the dataset. However, similar to previous studies on Rayleigh waves (Nicolson et al. 2012, 2014), initial experiments which used these measured uncertainties during tomographic inversion showed that their magnitude was too low (see Section 4.2). As mentioned above, in a second stage of our study we therefore assumed the level of data noise to be unknown and estimated it as one of the inversion parameters.

4 SEISMIC TRAVELTIME TOMOGRAPHY

We performed seismic tomography using traveltime measurements at 4, 6, 8, 9, 10, 11, 12, 15 seconds period and a fully non-linear transdimensional Markov chain inversion method in which rays are calculated at each step of the Markov chain. We created our non-linear tomography code by combining the original rj-McMC code of T. Bodin (as used in Bodin & Sambridge (2009)) with the fast-marching eikonal solver *fm2dss* from N. Rawlinson (Rawlinson & Sambridge 2004, 2005).

Within this section, we give an outline of the transdimensional inversion method for tomography and refer the reader to Bodin & Sambridge (2009) and Bodin et al. (2012a) for further details. We then describe a series of initial experiments which we performed by invert-

ing the 10 seconds period dataset using different forms of data noise parametrisation. These experiments allowed us to analyse the effect of different data uncertainty parametrisations on the final results, and to select distance-dependent uncertainty as the most suitable parametrisation for the inversions at 4–15 seconds. Finally, we present Love-wave group-velocity maps at all of the analysed periods and their associated maps of standard deviation.

4.1 Inversion method

In transdimensional traveltime tomography, the model is described by a tessellation of Voronoi cells of variable shape and size (as in Fig. 6(b)), and the inversion parameters include the number of such cells, their location and their velocity. After the initial tests described in Section 4.2, we chose to treat data noise as an additional unknown parameter and assumed traveltime uncertainties to be dependent on distance similarly to Bodin et al. (2012a):

$$\sigma_i = a \times d_i + b \tag{1}$$

where σ_i is the standard deviation (in seconds) of the traveltime uncertainty along raypath i, d_i is the source-to-receiver length of raypath i (here defined as the *actual* length in degrees of raypath i after ray tracing through the current model), as opposed to the length in some reference model, and a and b are hyperparameters to be estimated during inversion.

Our fully non-linear approach to transdimensional tomography consists of the following steps which are shown schematically in Fig. 6(a) and (b):

(i) An initial velocity model $\mathbf{m}$ is drawn from a uniform distribution of Voronoi-tessellated models with a uniformly-distributed number of cells, and uniformly-distributed seismic velocity and data noise parameters.

(ii) All raypaths and corresponding traveltimes are calculated through $\mathbf{m}$.

(iii) A new model $\mathbf{m}'$ is proposed by randomly perturbing the current model $\mathbf{m}$ (i.e., by changing either the velocity of a random Voronoi cell, a data noise hyperparameter, or the geometry of the model by either adding, deleting or moving a cell).

(iv) All raypaths and corresponding traveltimes are calculated through $\mathbf{m}'$.

(v) The acceptance ratio $\alpha(\mathbf{m}'|\mathbf{m})$ is calculated according to equation (18) in Bodin & Sambridge (2009) and the chain goes back to step (iii) after either accepting the proposed model $\mathbf{m}'$ with probability $\alpha(\mathbf{m}'|\mathbf{m})$, and otherwise rejecting it: if accepted, $\mathbf{m}'$ replaces $\mathbf{m}$ and becomes the new current model; if rejected, then $\mathbf{m}'$ is simply discarded.

This algorithm ensures that all models that improve the data fit are accepted, while those that do not are randomly accepted or rejected depending on their likelihood; also,

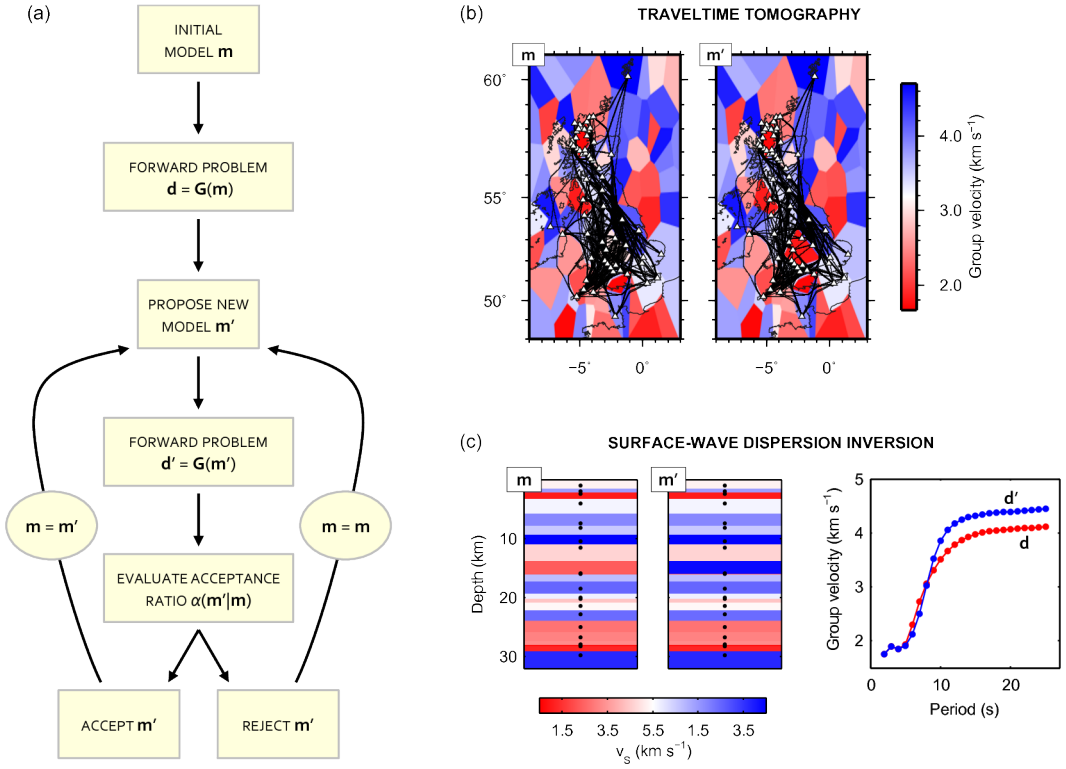

Figure 6. (a) Schematic workflow of the rj-McMC algorithm. (b) In the case of traveltime tomography, the model is parametrised by a tessellation of 2-dimensional Voronoi cells (tiles), and the forward problem consists of calculating all available raypaths and traveltimes through models $\mathbf{m}$ and $\mathbf{m}'$ at each step of the Markov chain. (c) In the case of surface-wave dispersion depth-inversion, the model is parametrised by a number of 1-dimensional Voronoi nuclei (the black dots in the model images) such that layer boundaries are equidistant to adjacent nuclei, and the forward problem consists of computing dispersion curves shown on the right, for $\mathbf{m}$ and $\mathbf{m}'$ at each step of the Markov chain.

thanks to the natural parsimony of Bayesian inference, overly complicated models are naturally (statistically) avoided (Bodin & Sambridge 2009). In addition, multiple Markov chains can be run independently by starting from different initial models, ensuring a larger portion of the model space is explored.

We solve the forward problem of ray tracing with an eikonal solver which uses the Fast Marching Method (FMM) to track the evolution of the seismic wavefront over a regular grid of points (Rawlinson & Sambridge 2004, 2005), and then to trace each raypath by following the gradient of the traveltime field. We defined a wavefront propagation grid by dividing each $1^\circ \times 1^\circ$ area into 16×16 cells, and applied a refined grid close to the sources by further dividing each cell within a distance of 0.5° from the source into 4×4 subcells. From our experiments, this grid parametrisation seemed to provide a good compromise between raypath accuracy

and computation time. The linearised method originally described by Bodin & Sambridge (2009) keeps raypaths fixed throughout each run of the inversion and updates them only between runs. We instead compute the ray geometry at each step of the Markov chain which ensures that the physics of ray propagation is never simplified, that the correct traveltimes are used in the estimation of the likelihood function, and that the correct ray path lengths are used in the data uncertainty estimation in equation 1. Although doing so dramatically increases the computation time, it prevents raypath- and parametrisation-related biases from being introduced into the final solution as demonstrated by Galetti et al. (2015).

4.2 Traveltime uncertainty parametrisation

Traveltime uncertainties are a fundamental part of seismic traveltime datasets as they define how accurately the observed traveltimes should be fit during tomography. Within a transdimensional framework, the use of correct uncertainty measurements is particularly important with regards to the posterior on the number of model parameters, as the magnitude of the data uncertainties directly influences the number of parameters required to fit the data and hence the complexity of the solution. One of the apparent advantages of ambient-noise tomography compared to more traditional earthquake tomography methods is the ability to estimate traveltime uncertainties from the variability of the interferometric Green's functions in time. As an example, Lin et al. (2007) and Yang et al. (2007) used 3-month stacks of cross-correlations to analyse the repeatability of interferometric Green's functions and estimate uncertainty in the dispersion measurements. However, more recent studies by Nicolson et al. (2012, 2014) showed that the same approach on a Rayleigh-wave dataset from the British Isles yielded traveltime uncertainties that were lower than expected. Hence, although a number of tomography studies have been conducted successfully using Green's functions from ambient noise and associated uncertainties estimated in this way, it is still unclear how exactly uncertainties in ambient-noise datasets should be quantified, and research on this topic is ongoing.

Within this section, we describe a number of experiments that we conducted while testing the fully non-linear rj-McMC algorithm described above with different types of data noise parametrisation. The results of these experiments highlight the impact of data uncertainties on the final solution, and may provide guidelines for future studies. In all of the following experiments, we inverted the same 10 second period traveltime dataset by running 16 parallel Markov chains for 3×10^6 iterations each, discarding the first 5×10^5 samples as burn-in and only retaining every 500^{th} sample in the solution ensemble. We gave uniform priors to cell velocities (Table 1), number of cells (10–300) and noise hyperparameters (when present).

Period (s)	v_{avg} (km s^{-1})	θ_v (km s^{-1})
4	3.1720	1.7224
6	3.0464	1.5707
8	3.0701	1.5093
9	3.1218	1.5652
10	3.1847	1.6211
11	3.2292	1.3436
12	3.2482	1.2045
15	3.3239	1.1965

Table 1. Average velocity (v_{avg}) and upper and lower velocity range (θ_v) used to define the velocity prior at each of the analysed periods. At each period, the lower and upper bounds of the uniform velocity prior are given by $v_{min} = v_{avg} - \theta_v$ and $v_{max} = v_{avg} + \theta_v$, respectively.

We performed an initial inversion using the traveltime uncertainties obtained from picking travel times on four (for the RUSH-II dataset) and five (for the rest of the UK-wide network) independent random stacks of daily cross-correlations. The average 10 second group-velocity map and the posterior distribution on the number of cells obtained in this case are shown in Figs 7(a) and (e), respectively. Although the velocity map shows realistic features which correlate with the known geology, the number of parameters needed to constrain the velocity model is very high, with the majority of samples having a number of Voronoi cells that falls at the higher end of the prior distribution. We also found that similar posterior distributions were obtained for priors with significantly higher upper bounds, hence this is unlikely to be due to our particular choice of prior being too narrow. In transdimensional tomography, the number of Voronoi cells needed to constrain the data is directly affected by the level of data noise (Bodin et al. 2012a): since the data are fit to within their levels of uncertainty, large traveltime uncertainties produce simpler models with fewer Voronoi cells, while small uncertainty values cause more cells to be added into the model, improving the data fit but increasing the model complexity. The effect observed in Fig. 7(e) can therefore be explained as a consequence of the measured traveltime uncertainties being too small and the data being over-fitted.

A similar behaviour was observed in fixed-dimensional tomography by Nicolson et al. (2012) and Nicolson et al. (2014). They used a linearised inversion method to produce a set of Rayleigh-wave tomographic maps of the British Isles at various periods using different combinations of damping and smoothing. They then calculated the weighted root-mean-square

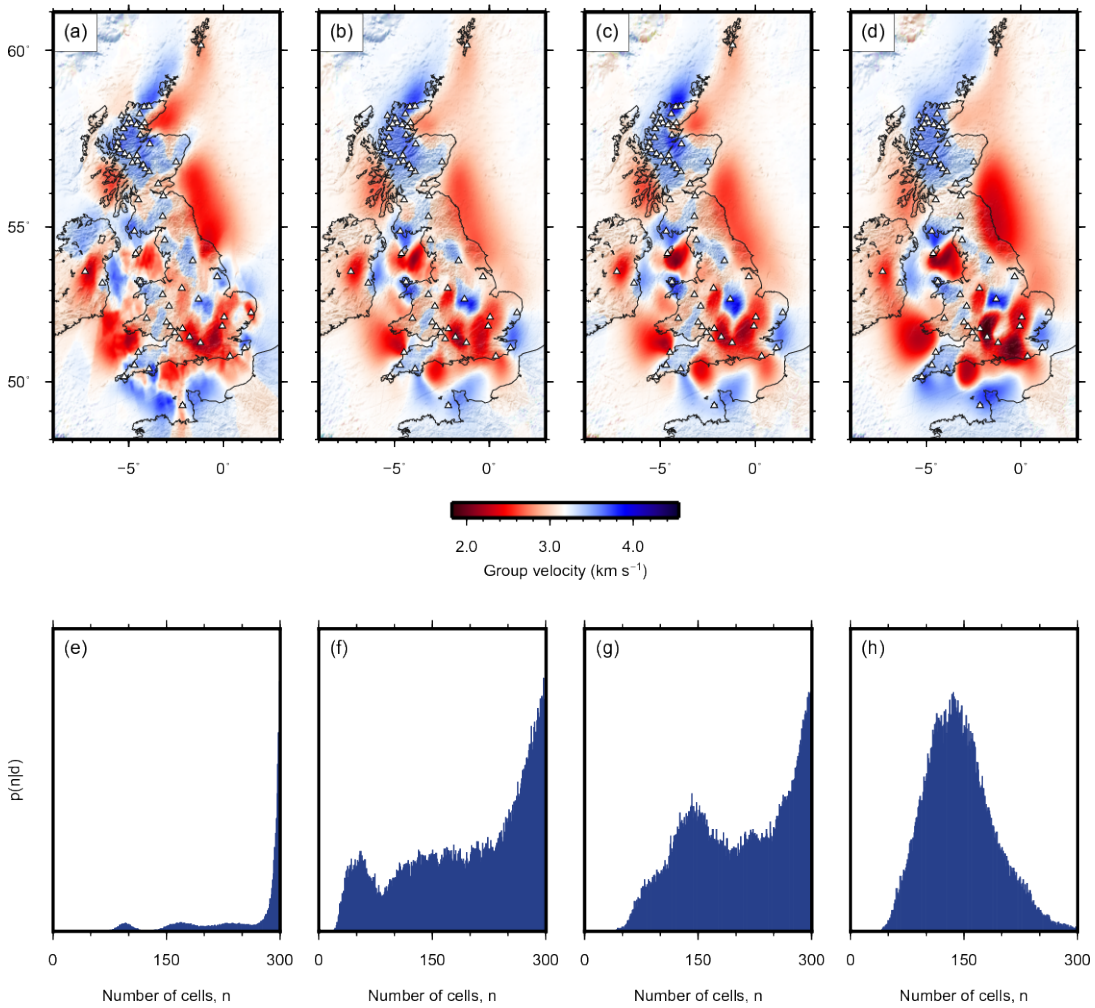

Figure 7. Average Love-wave group-velocity maps and posterior distributions on number of cells, obtained from transdimensional tomography at 10 seconds period with different data noise parametrisations. (a) and (e): traveltime uncertainties are measured from random stacks of noise cross-correlations. (b) and (f): traveltime uncertainties are estimated by multiplying those measured from random cross-correlations stacks by scaling factor λ, which is estimated during inversion. (c) and (g): traveltime uncertainties are estimated by multiplying those measured from random cross-correlations stacks by scaling factors λ_1 (for RUSH-II stations) and λ_2 (for the UK-wide array), which are estimated during inversion. (d) and (h) traveltime uncertainties are assumed to vary with source-to-receiver distance, and are parametrised according to equation 1.

of the data residuals (RMS_W) for each map, a dimensionless quantity which provides a measure of the normalised misfit of the post-inversion modelled data:

$$RMS_W = \sqrt{\frac{1}{N}\sum_{i=1}^{N}\frac{x_i^2}{\sigma_i^2}}\,, \tag{2}$$

where N is the number of raypaths, and x_i and σ_i are the traveltime residual and uncertainty

associated with raypath i, respectively. As the RMS_W includes a ratio of traveltime residuals to uncertainties, values which are significantly greater than 1 denote solutions that are more affected by the regularisation parameters than the data fits (and which should therefore be discarded), while an RMS_W which is less than 1 indicates that the observed traveltimes fit the solution to within data uncertainties. Nicolson et al. (2012, 2014) obtained RMS_W values greater than 1 even when no regularisation was applied during their inversions for models using a very dense regular grid of velocity nodes, indicating that the level of data uncertainties estimated with this method may not have been sufficiently large to account for both observational and modelling errors.

We therefore tried inverting the same traveltime dataset by multiplying the measured uncertainties by scaling factor λ whose value was estimated as one of the inversion parameters:

$$\sigma_i^{post} = \lambda \times \sigma_i^{prior} \ , \tag{3}$$

where σ_i^{prior} and σ_i^{post} are the prior and posterior uncertainty for path i, respectively, and λ is a parameter to be estimated. A uniform prior between 0.2 and 8 was chosen for λ, and to evaluate the effect of the combination of the two disconnected datasets (RUSH-II and the rest of the UK-wide network) inversions were performed first for a single λ for both datasets and then for two separate values of λ, one for each dataset. Average velocity maps and posteriors on the number of cells are shown in Figs 7(b) and (f) for a single λ, and in Figs 7(c) and (g) for two separate λ values. Although the velocity maps in Figs 7(b) and (c) show similar structures to those observed in the previous case (Fig. 7(a)), the posteriors on the number of cells show a significant reduction in the number of parameters needed to constrain the structure, as some of the data are no longer over fitted. In both cases, the posteriors on λ (Figs 8(a) and (b)) peak at values which are greater than one, confirming that the uncertainties measured from the independent cross-correlation stacks should be scaled to larger values. In particular, Fig. 8(b) shows that the magnitude of scaling factor λ is expected to be around 1 for the RUSH-II dataset (purple), while it peaks around 3 for the UK-wide array (green), suggesting that the magnitude of the measured uncertainties is significantly different in the two datasets. This is consistent with the findings of Nicolson et al. (2012, 2014), who showed that the uncertainty estimation method of Lin et al. (2007) seemed to work better for a study across the Scottish Highlands which used Rayleigh-wave data from the RUSH-II network (Nicolson et al. 2012), while it appeared to have flaws when applied over the whole of the British Isles using a similar array of stations to the UK-wide deployment from this study (Nicolson et al. 2014). Nevertheless, Figs 7(f)–(g) show that the majority of models are still characterised by a very

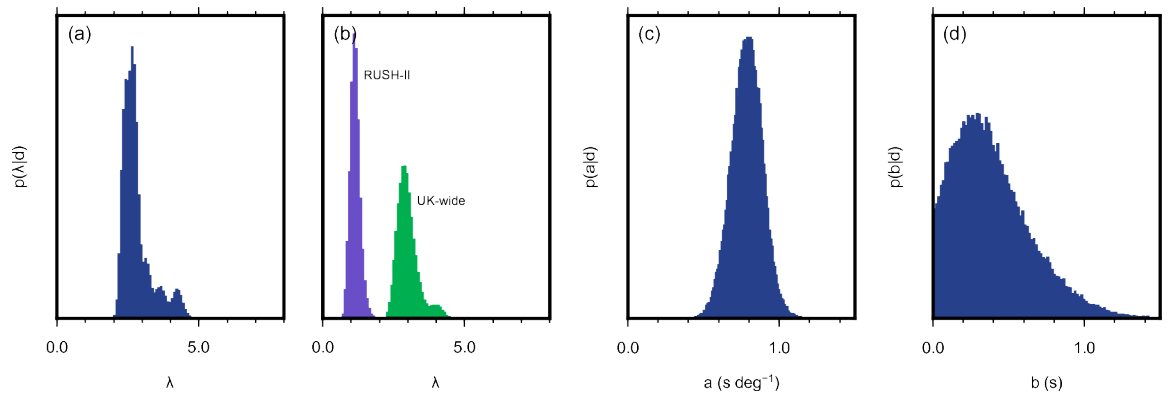

Figure 8. Posterior PDF on noise hyperparameters (a) λ for RUSH-II and UK-wide arrays combined, (b) λ for separate RUSH-II and UK-wide arrays, (c) a and (d) b.

large number of Voronoi cells that tends to the upper bound of the prior, suggesting that the scaled uncertainties are still not large enough to be considered reliable.

Finally we performed the inversion by assuming data noise proportional to source-to-receiver distance as in equation 1 across the data from all networks: uniform priors were chosen for a (0.3–1.2 deg s^{-1}) and b (0.0–1.5 s). The average velocity map and the posterior distribution on the number of cells are shown in Figs 7(d) and (h), respectively. The posteriors on noise hyperparameters a and b are shown in Figs 8(c) and (d), respectively. Although the overall velocity structures are comparable to those observed in the previous cases, the posterior on the number of cells shows that traveltimes are correctly fitted up to the estimated uncertainty values with far fewer cells. For this reason, we chose this data noise parametrisation to invert seismic traveltimes at all of the other analysed periods.

Overall, the four velocity maps in Fig. 7 display similar high- and low-velocity features which agree with one another and with the known geology of the area (see Section 4.3). However, the magnitude of these structures appears to be strongly influenced by the data noise parametrisation employed during inversion. In particular, the magnitude of the velocity structures observed in Fig. 7(a) appears to be lower than in the other cases (compare for instance the East Irish sea low-velocity anomaly near $-4°$E, $54°$N, and the high-velocity anomaly near $-1°$E, $52.5°$N), and the large number of Voronoi cells in the posterior causes the boundaries between low- and high-velocity structures to look 'staggered', as some of the sharp Voronoi cell boundaries are still visible. This does not seem to happen in the average map of Fig. 7(d), which looks smoother and does not reveal the presence of Voronoi cells in the ensemble models. In general, an increase in the smoothness of the average map can be observed from left to right in the top row of Fig. 7, even though on average fewer cells are

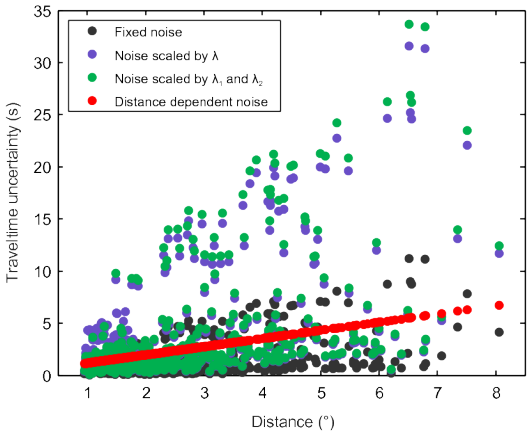

Figure 9. Measured and estimated traveltime uncertainties in the four noise parametrisation cases analysed. Black circles: traveltime uncertainties measured from random stacks of noise cross-correlations. Purple circles: traveltime uncertainties estimated by multiplying those measured from random cross-correlation stacks by the average value of scaling factor $\lambda = 2.81$ (from Fig. 8(a)). Green circles: traveltime uncertainties estimated by multiplying those measured from random cross-correlations stacks by the average values of scaling factors $\lambda_1 = 1.14$ (for RUSH-II stations) and $\lambda_2 = 3.00$ (for the UK-wide array) (from Fig. 8(b)). Red circles: traveltime uncertainties are assumed to vary with source-to-receiver distance and are parametrised according to equation 1 using the average values of $a = 0.79$ (from Fig. 8(c)) and $b = 0.39$ (from Fig. 8(d)).

used in 7(d) than in 7(a)–(c); this can be related to an improvement in the estimation of the number of parameters needed, which in turn may be connected to a more appropriate estimation of traveltime uncertainties. The measured and estimated traveltime uncertainties in the four cases analysed are plotted in Fig. 9 as a function of distance.

Plots showing the variation of the number of cells throughout the Markov chain can also provide useful information on convergence, which can be assumed to have been reached when the number of Voronoi cells becomes relatively stationary around the region of highest probability. Figure 10 displays the number of Voronoi cells versus sample number for all Markov chains run in the four cases discussed above. It shows that convergence is not reached by the end of the Markov chains in the first three cases above (Figs 10(a)–(c)), while it is reached within a few hundred thousand iterations when data noise is parametrised according to equation 1 (Fig. 10(d)). A similar behaviour was observed on plots of noise parameters versus iteration number (not shown).

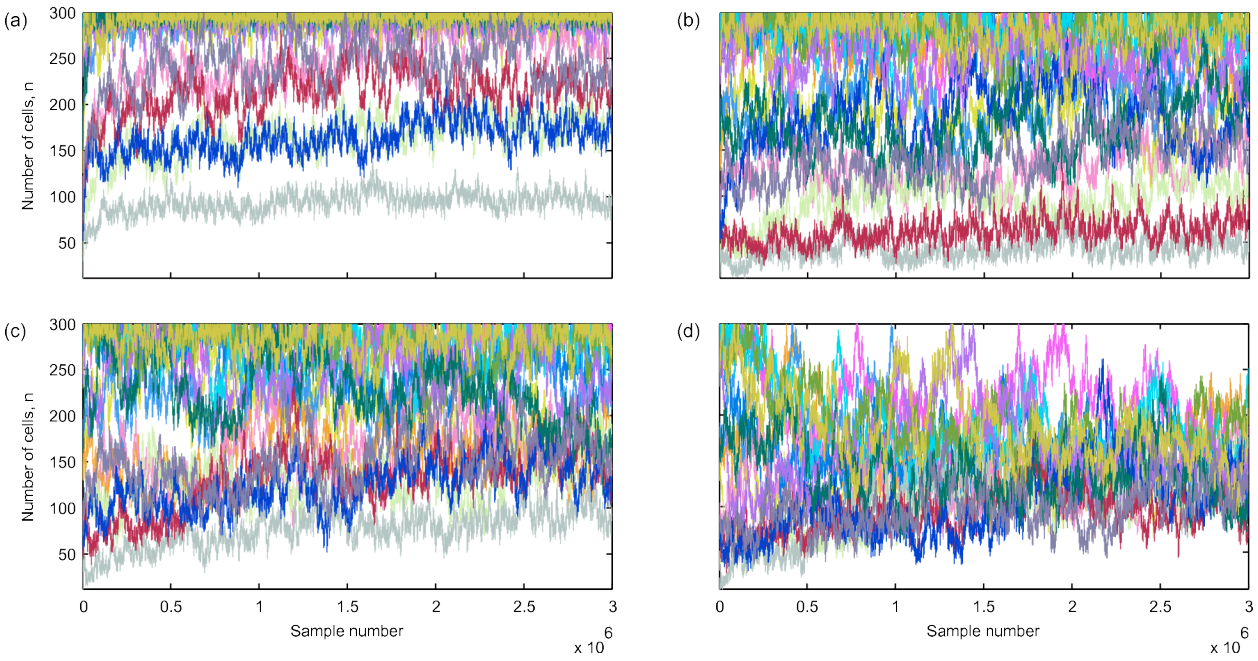

Figure 10. Number of Voronoi cells versus iteration number on each of the 16 Markov chains run for the four experiments in Fig. 7: (a) traveltime uncertainties are measured from random stacks of noise cross-correlations; (b) traveltime uncertainties are estimated by multiplying those measured from random cross-correlations stacks by scaling factor λ, which is estimated during inversion; (c) traveltime uncertainties are estimated by multiplying those measured from random cross-correlations stacks by scaling factors λ_1 (for RUSH-II stations) and λ_2 (for the UK-wide array), which are estimated during inversion; (d) traveltime uncertainties are assumed to vary with source-to-receiver distance and are parametrised according to equation 1.

4.3 Love-wave group-velocity maps

Within this study, we ran 16 independent Markov chains in parallel to perform traveltime tomography at 4, 6, 8, 9, 10, 11, 12, 15 seconds period using traveltimes calculated along the inter-station paths shown in Fig. 11 (plotted for a constant-velocity model). We chose uniform priors for the number of Voronoi cells (10–400), cell velocity and location, and hyperparameters a (0.3–3.0 deg s^{-1}) and b (0.0–2.0 s). The cell velocity prior was chosen by measuring the average velocity across all valid paths at each period and providing upper and lower velocity bounds which exceeded the range of velocities observed on the dispersion curves. All Markov chains were run by performing 3 million iterations, and every 500$^{\text{th}}$ sample after a burn-in period of 5×10^5 iterations was included in the final (posterior) ensemble. As a means of quality control, we analysed plots similar to those in Fig. 10 to identify Markov chains which displayed an anomalous behaviour and removed them from the analysed ensemble (since occasionally

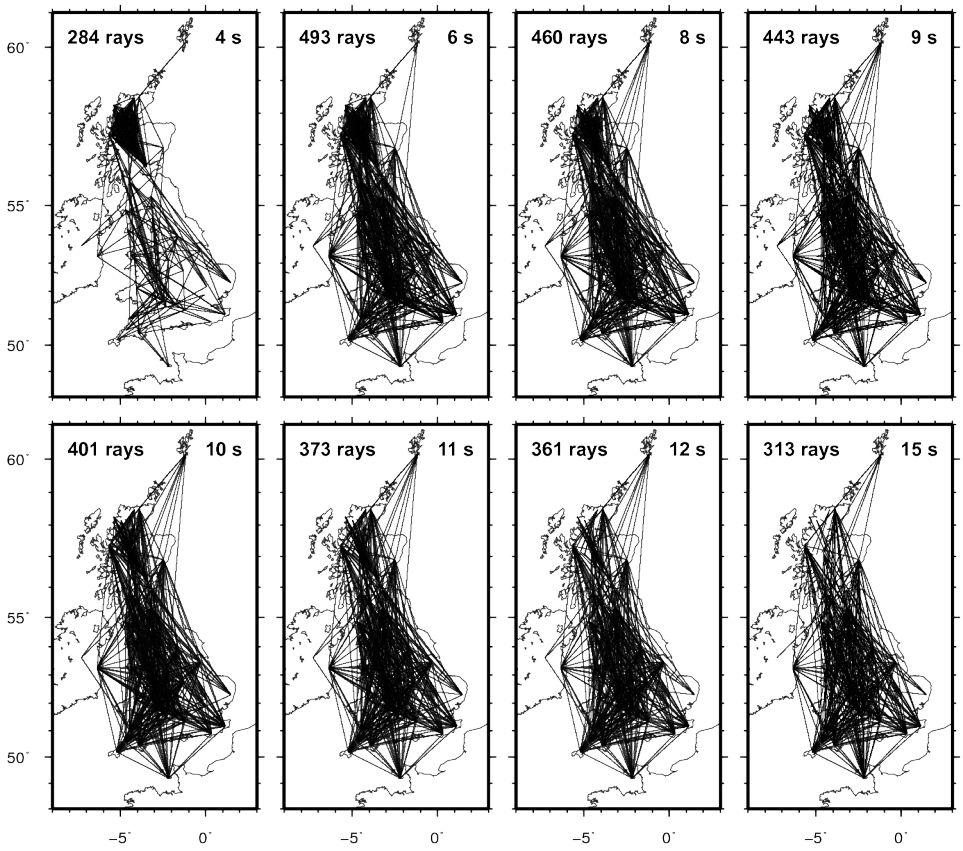

Figure 11. Raypaths used for tomography at all of the analysed periods. Note how the density of raypaths is particularly uneven across the imaged area.

individual chains got stuck in local minima from which they clearly could not escape within the available number of iterations). Average velocity models and maps of standard deviation were calculated from the model ensemble, together with posterior distributions on number of cells, noise hyperparameters a and b, and velocity at each point.

Average velocity and standard deviation maps at all of the analysed periods are shown in Figs 12 and 13, respectively. These were calculated by first defining a regular grid of geographical points with a spacing of $1/16^{\text{th}}$ of a degree in latitude and longitude, and then computing the average group velocity and its standard deviation across the ensemble of Voronoi models at each grid point location. In order to ease the comparison of velocity structures and uncertainties between the various periods, the same color scales are used across all average and standard deviation maps.

The group-velocity maps in Fig. 12 display the average group-velocity at each geographical point across the ensembles of Voronoi velocity models. Despite the ensemble models being parametrised by Voronoi cells, the average maps are smooth and do not show any trace of the

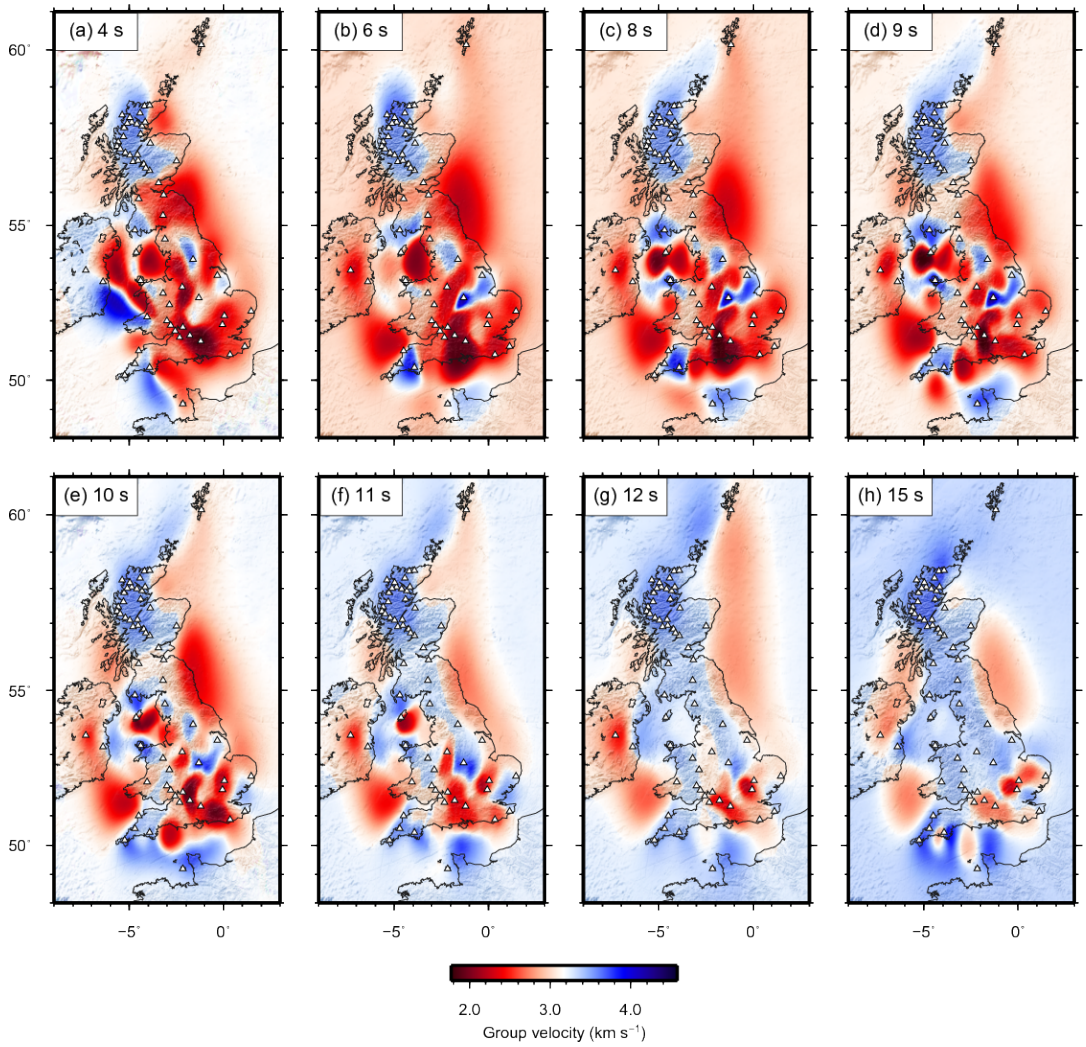

Figure 12. Mean Love-wave group-velocity maps of the British Isles from transdimensional ambient-noise tomography at (a) 4 s, (b) 6 s, (c) 8 s, (d) 9 s, (e) 10 s, (f) 11 s, (g) 12 s, (h) 15 s period.

Voronoi cell geometry. In general, an increase in group velocity is observed with increasing period, reflecting the general tendency of seismic velocity to increase with depth. The only exception to this trend is given by the 4 second average map, whose average velocity is larger than those observed at both 6 and 9 seconds period. This is likely due to the fact that most raypaths at 4 seconds are located in the Scottish Highlands (see top-left plot in Fig. 11), which are well known for being a region of high velocity due to their metamorphic origin.

The average maps can be used to identify various geological features at relatively shallow depths in the British Isles, with rocks of sedimentary origin being generally shown as low-velocity regions while igneous and metamorphic complexes are normally displayed as high velocities. The velocity maps in Figure 12 show a good correlation between the visible structures and the geology of the area (e.g., see Fig. 14 for tomography at 10 seconds period),

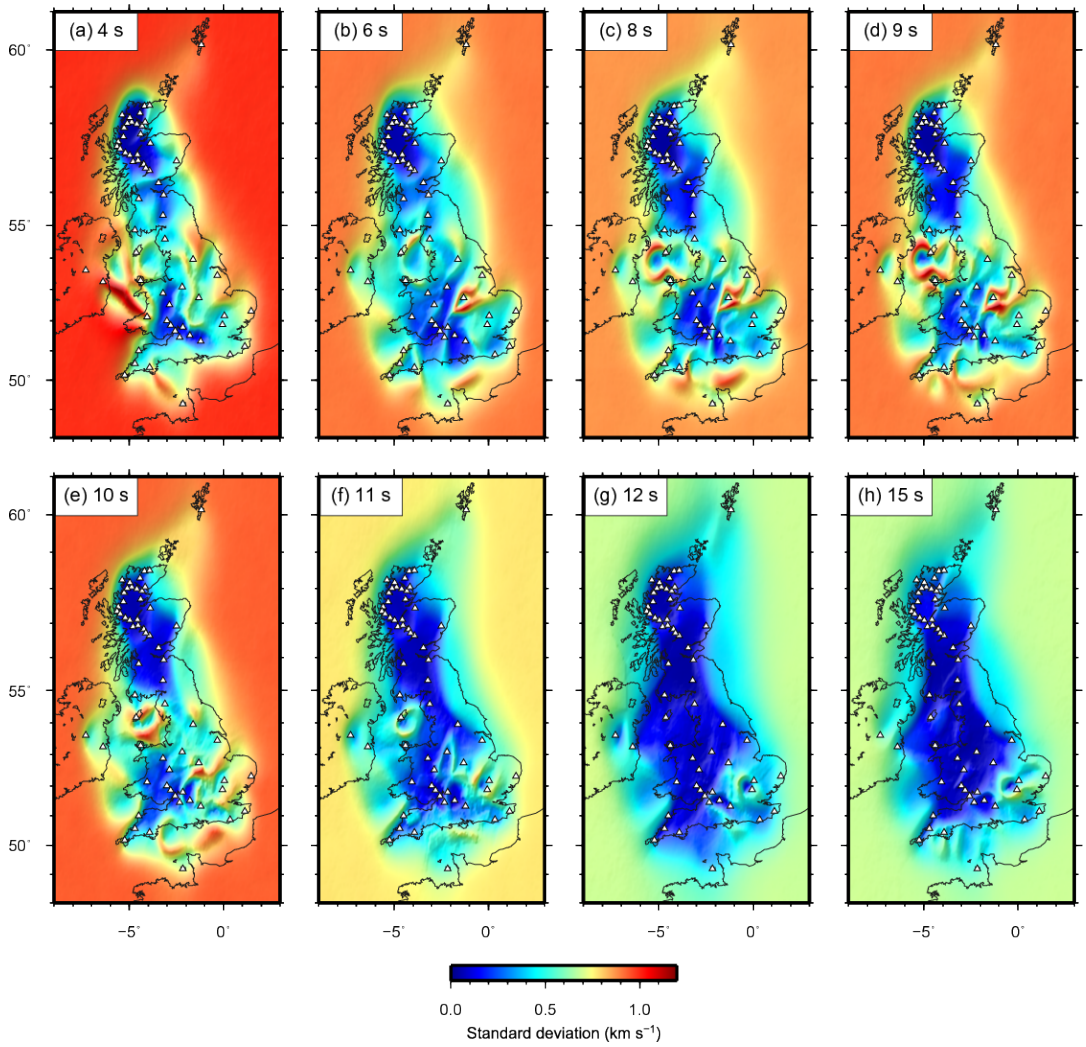

Figure 13. Standard deviation maps associated with each mean Love-wave group-velocity map in Fig. 12.

together with a general increase in the average group-velocity and a decrease in the number of visible features with increasing period.

Between 4 and 10 seconds period, the Lewisian and Dalradian complexes in the Scottish Highlands are clearly visible as regions of high seismic velocity, which is consistent with their crystalline metamorphic origin. High velocities in northern Britain also mark the accretionary complex of the Southern Uplands, following a SW-NE trend in the south of Scotland around $-4°$E, 55°N. The same trend is followed by the Midland Valley, which can be identified as the low-velocity zone around $-3.5°$E, 55.5°N, bounded by the Highland Boundary Fault to the north and the Southern Uplands Fault to the south (see Fig. 1(a)). Low seismic velocities can also be observed in off-shore sedimentary basins such as the Firth of Forth and the Moray Firth. In northern England, the limestones of the Pennines can be identified by a high-velocity

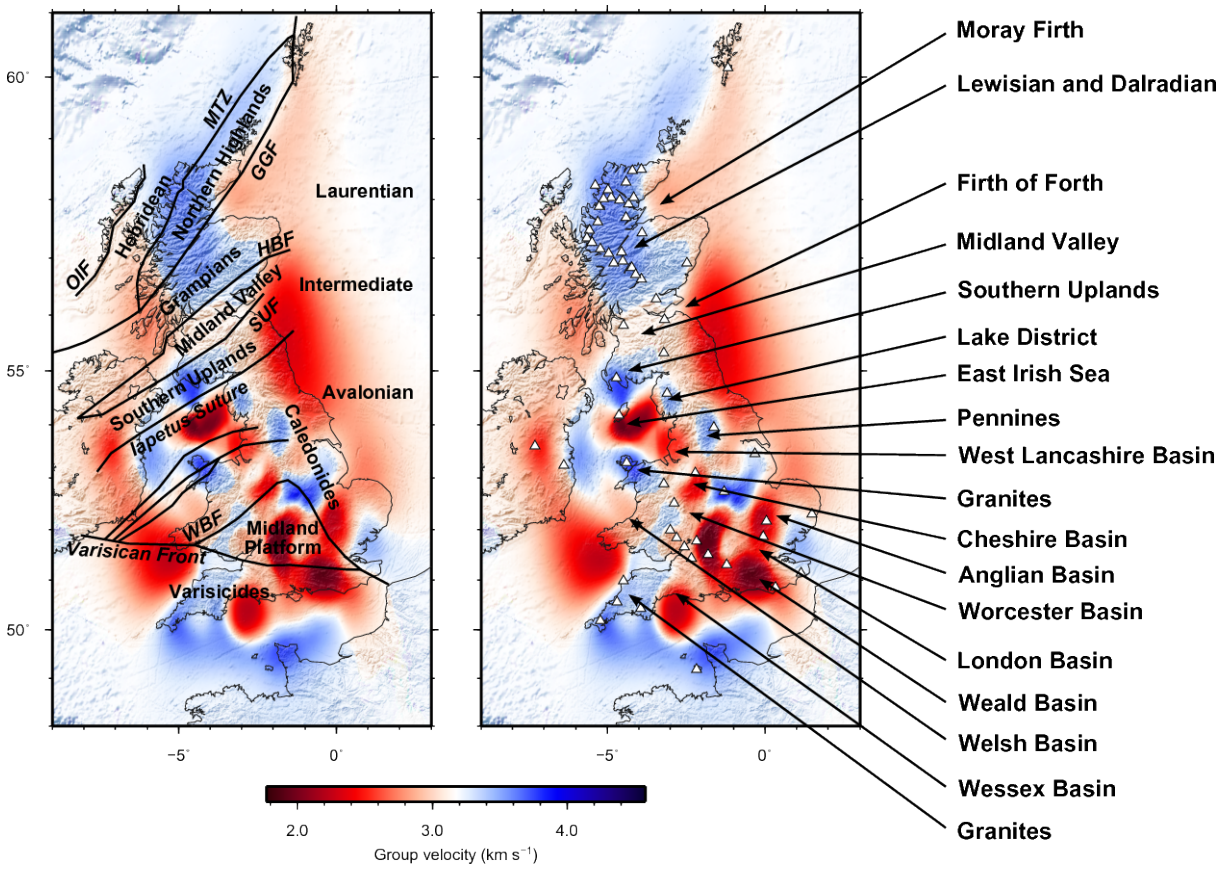

Figure 14. Mean Love-wave group-velocity map of the British Isles from transdimensional ambient-noise tomography at 10 seconds period. The terrane boundaries from Fig. 1 are overlaid on the the left-hand map, and the main geological structures are indicated on the right-hand map.

region following an approximately north-south trend around −2°E, 54°N. Similarly, the Lake District corresponds to an area of higher than average velocity (around −3°E, 54.5°N), and the granitic intrusions in Cornwall (around −4.5°E, 50.5°N) and north-west Wales (around −4°E, 53°N) are also marked by high seismic velocities. The Midland Platform has been found to be an area of high crustal thickness by a number of authors (Chadwick & Pharaoh 1998; Tomlinson et al. 2006) and can be observed as a region of lower than average velocity in the south of England (around −2°E, 52°N). Low velocities are also found in a number of sedimentary basins such as the East Irish Sea (around −4.5°E, 54°N), the London Basin at the south-east corner of the Midland Platform (around 0°E, 51.5°N), the Anglian Basin east of the Midland Platform (around 0°E, 52°N), the Wessex-Weald basin south of the Varisican Front (around −2.5°E, 51°N and 0°E, 51°N), and the Welsh, Cheshire, Worcester and West Lancashire Basins lying to the north and west of the Midland Platform.

The high-velocity feature in the East Midlands (around −1°E, 53°N) was previously ob-

served in Rayleigh-wave tomography studies of the area by Nicolson et al. (2014), who related it to the northern limit of the Anglo-Brabant Massif. This feature also emerged when experimental inversions at 6 seconds period were performed by removing either station CWF (located in the middle of the anomaly at most periods - see Fig. 2) or station LMK (located on the north-eastern edge of the anomaly - see Fig. 2) from the dataset, hence it is robust and cannot be due only to the data recorded at these two stations. Surface geology around station CWF includes ancient volcanic breccias, and evidence from gravity and magnetic data suggests that granitic batholiths and dykes underlie an area to the east of CWF, which may explain the origin of this high-velocity feature. Alternatively, the anomaly may be interpreted as evidence of Proterozoic basement in an area of thin sedimentary cover. However, more detailed studies are currently needed in order to understand the exact origin of this feature.

Between 11 and 15 seconds period the various sedimentary basins progressively disappear as the depth to which these periods are sensitive increases. The low-velocity anomaly associated with the East Irish Sea basin decreases in size between 4 and 11 seconds period and is no longer visible at 12 seconds period. Similarly, the low velocities found in the Midland Valley become less pronounced as period increases, and the formation becomes essentially undistinguishable from the neighbouring high-velocity complexes at 12 seconds period. Since the thickness of the Midland Valley sediments is suggested to be between 4 and 8 km (Dentith & Hall 1989, 1990), the 12 and 15 seconds maps are therefore likely to be at least as representative of the basement rocks below this depth rather than only of the overlying sediments. In contrast, the sedimentary basins in the south of England decrease in size but are still visible between 11 and 15 seconds period.

The uncertainty maps in Fig. 13 display the standard deviation of group-velocity across the ensemble of Voronoi velocity models, and provide an indication of how well the velocities in the average maps are constrained. From these plots it is evident that the magnitude of the uncertainties depends on both raypath coverage and underlying velocity structure, as well as on the employed velocity prior distribution. Off-shore uncertainties are large due to the lack of raypaths in marine areas and in most cases are equal to their a priori values which decrease with increasing period due to a reduction in the range between the minimum and maximum a priori group-velocity (see parameter θ_v in Table 1). Within the regions interrogated by raypaths, the magnitude of uncertainties presents large variations across the range of analysed periods. In general, group-velocity standard deviations appear to decrease as period increases, perhaps due to a reduction in the lateral heterogeneity of the subsurface, with periods above 11 seconds being mainly sensitive to basement structures. Between 4 and 10 seconds, uncertainties

are lower in Scotland and south-west England due to the denser ray coverage, while they are higher in the north of England and along the west coast of mainland Britain where raypath density is lower. In addition, loop-like structures with large standard deviation similar to those discussed by Galetti et al. (2015) can be observed surrounding the low-velocity anomaly in the East Irish Sea (near −4°E 54°N), various low-velocity anomalies in the south of England (near −3°E 50.5°N, 0°E 52°N, −5.5°E 51.5°N), and a high-velocity anomaly near −1°E 53°N. At 11 seconds period, uncertainties decrease in magnitude and are relatively uniform across mainland Britain, with the exception of the high-uncertainty loops near −4°E 54°N, −2°E 52.5°N and 0°E 52°N. At 12 and 15 seconds period, uncertainties are relatively low and uniform across the investigated area, with the exception of the high-uncertainty loop surrounding the low-velocity anomaly near 0°E 52°N.

5 LOVE-WAVE GROUP-VELOCITY DEPTH INVERSION FOR SHEAR VELOCITY STRUCTURE

Although it is well known that group-velocity maps at increasing periods are representative of increasingly greater depths within the Earth, such maps do not provide a good indication of the depth of the observed structures as they only yield average velocities over a range of depths. Hence, a further step must be taken after tomographic inversion in order to relate velocity structures to actual depths in the Earth's subsurface. A common way to achieve this involves producing a set of group-velocity dispersion curves by sampling the 2D average group-velocity and standard deviation maps at all of the analysed periods over a regular grid of geographical points. A dispersion curve can then be constructed at each geographical point by taking group-velocity measurements from the 2D average maps and uncertainty values from the 2D standard deviation maps at the available periods. Each dispersion curve may then be inverted independently for a 1D shear-velocity (v_S) profile since Love-wave group velocities are primarily sensitive to shear velocity variations; by repeating the inversion for each available dispersion curve (i.e., each available geographical point) a 3D v_S model of the crust may be obtained.

In the second part of our study, we therefore used the results of traveltime tomography to produce 3D shear-velocity models of the crust. Since this was extremely expensive computationally we focussed on a particular sub-region of the British Isles. In this section we provide an overview of the inversion method and present the crustal structure of the East Irish Sea sedimentary basin.

5.1 Inversion method

We discretised the average group-velocity and standard deviation maps presented in the previous section over a regular grid of geographical points with a spacing of $1/16^{\text{th}}$ of a degree. As a means of quality control, we used the standard deviation maps from tomography to remove dispersion measurements with excessively large uncertainty from the dispersion dataset. At each of the analysed periods, the a priori uniformly-distributed standard deviation σ^{prior} on group-velocity can be expressed as

$$\sigma^{prior} = \sqrt{\frac{(v_{max} - v_{min})^2}{12}}\,, \tag{4}$$

where v_{min} and v_{max} are the lower and upper bounds on the group-velocity prior, respectively (see Table 1). Since a posterior standard deviation value near σ_{prior} indicates that no additional information was obtained on group velocities from tomography, we constructed dispersion curves using only those points having a posterior standard deviation less than 75% of σ_{prior}. This means that different dispersion curves (hence different geographical points at which a dispersion curve was constructed) had different numbers of data points, with a minimum of 2 considered as a candidate for subsequent analysis (Fig. 15). As expected, no dispersion curves were constructed in off-shore areas where resolution is low, and dispersion curves with the largest number of data points were constructed on mainland Britain where the density of raypaths is largest. In total, 14665 dispersion curves were produced over the entire imaged area, and a subset of 2145 curves was used for the inversion in the East Irish Sea basin (denoted by the box in Fig. 15).

Similarly to tomography, we used the rj-McMC algorithm to solve the inverse problem to estimate shear velocity structure with depth. In fact, the concept of transdimensionality is not limited to traveltime tomography but can be adapted to a number of different inverse problems including regression (Gallagher et al. 2011), inversion of controlled source electromagnetic data (Ray et al. 2014), inversion of surface-wave dispersion data (Young et al. 2013), and joint inversion of surface-wave dispersion and receiver function data (Bodin et al. 2012b). In all of these cases, rather than obtaining a single 'best-fit' model which might be heavily influenced by the choice of model parametrisation, the solution is represented by an ensemble of millions of samples, all of which fit the recorded data to within uncertainties, and a suitable family of parametrisations is inferred from the data during the inversion.

The workflow of the rj-McMC algorithm for group-velocity inversion resembles that of tomography described in Section 4.1, and is illustrated in Fig. 6(a) and (c). The layered model is described by a series of 'Voronoi nuclei' (the black dots in Fig. 6(c)) which are assigned a

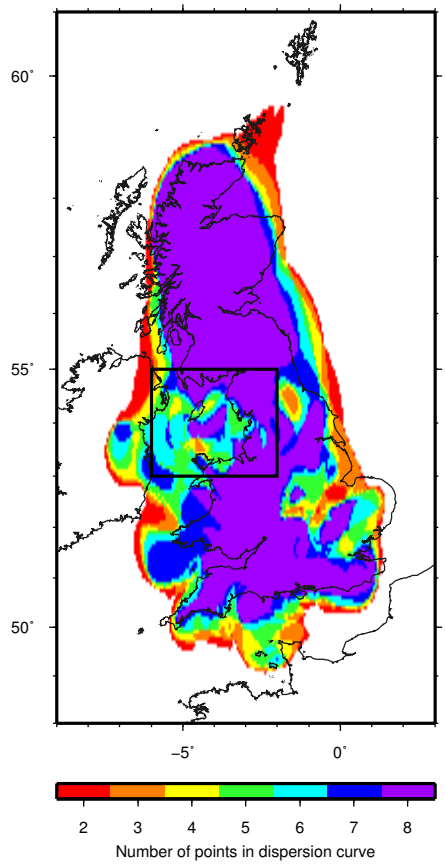

Figure 15. Number of valid (> 2) dispersion data points at each geographical location in the British Isles. The box denotes the extent of the area around the East Irish Sea basin for which Love-wave group-velocity inversion was performed.

depth and a v_S value. The vertical position of the collection of Voronoi nuclei determines the thickness and depth of the uniform horizontal layers. Note that each Voronoi nucleus is not necessarily located at the centre of its corresponding layer, but rather each layer boundary is equidistant to its two adjacent nuclei. Similarly to its traveltime tomography equivalent, this method uses Bayes' theorem and Markov chain Monte Carlo to produce an ensemble of layered models $\mathbf{m}$ which are distributed according to the posterior distribution. Prior distributions are given on the depth of Voronoi nuclei, number of layers and layer velocity. Data noise may also be parametrised by defining a hyperparameter γ which serves as a scaling factor for the a priori uncertainties (similar to equation 3) and which can be estimated during the inversion. As in the case of traveltime tomography with variable data noise, this ensures that the posterior on the number of parameters (i.e., layers) is not adversely affected by the absolute value of the noise level, and that data uncertainties account for both observational and modelling errors.

The initial model $\mathbf{m}$ is generated randomly, and subsequent models $\mathbf{m}'$ are proposed by randomly perturbing one of the parameters of $\mathbf{m}$ (i.e., adding/deleting/moving a layer, changing a layer's velocity, or changing the data noise hyperparameter γ). The proposed model $\mathbf{m}'$ is either accepted or rejected depending on its likelihood: if it improves the data fit, it is accepted; if it worsens the data fit, it is randomly accepted or rejected according to acceptance probability $\alpha(\mathbf{m}'|\mathbf{m})$. When the proposed model $\mathbf{m}'$ is accepted, it replaces $\mathbf{m}$ as the current model, and the chain continues. At the end of the Markov chain, the first few hundred thousand samples are discarded as 'burn-in', and only every two hundredth model is retained in the analysed ensemble to ensure that the samples are approximately uncorrelated. The results of the 1D inversion can then be visualised as 2D posteriors of v_S probability versus depth, or as 1D average or maximum-probability profiles of v_S. In addition, posteriors on the location of discontinuities, number of layers, and noise hyperparameter γ may be obtained.

In group-velocity inversion, the forward problem consists of calculating Rayleigh- or Love-wave group-velocities for a given layered velocity model. We solved the forward problem using the DISPER80 subroutines by Saito (1988), which require values for compressional velocity v_P, shear velocity v_S and density ρ to be defined for each layer in order to compute group velocities. In this study, we varied v_S during inversion, keeping the v_P/v_S ratio fixed to a typical crustal value of 1.76, and density was assumed to be dependent on v_P as in Kurita (1973):

$$\rho = 2.35 + 0.036 \times (v_P - 3.0)^2 \, . \tag{5}$$

Although the DISPER80 forward modelling subroutines are fast, are popular amongst seismologists, and therefore to some extent are ideal for use in a Monte Carlo scheme, they may produce incorrect dispersion curves when relatively unusual models are proposed. For instance, we found that the code produced unreliable results when a particularly low-velocity layer was present at very large depths or when the half-space had lower velocity than the layers above, as might happen when models are generated randomly. Examples of some of these tests are shown in Fig. 16, where DISPER80 is used to compute Love-wave group-velocity dispersion by using a fixed value of 1.76 for v_P/v_S, and by letting density vary as a function of v_P as in equation 5.

Consider first the case of a velocity profile in which v_S generally increases with depth, as illustrated in Fig. 16(a). The blue shear-velocity profile in panel (a) produces the Love-wave group-velocity dispersion curve denoted by the blue circles in panel (b). When the shear-velocity of the layer near 65 km depth is perturbed by +1% (red profile in (a)), the dispersion curve denoted by the red asterisks in panel (b) is obtained. As expected, since the

amount of velocity perturbation is small and is applied at a large depth at which the analysed periods have very little sensitivity, the group velocities obtained in the two cases match almost perfectly. The case of an inverted velocity profile, in which a layer of particularly low velocity is present at large depths, is illustrated in Fig. 16(c). As in the previous case, the blue shear-velocity profile in panel (c) produces the Love-wave group-velocity dispersion curve denoted by the blue circles in panel (d). When the shear-velocity of the layer near 65 km depth is perturbed by +1% (red profile in (c)), the dispersion curve denoted by the red asterisks in panel (d) is obtained. In this case, although the amount of perturbation is of the same order of magnitude as that in the previous example, the change in group velocities is larger than 1%. Given the large depth at which the perturbation was applied and that the sensitivity of the analysed periods at the perturbation depth should be very limited, this large change is likely to be due to errors introduced by the DISPER80 modelling code.

Although models such as the one in Fig. 16(c) might be relatively unusual in real scenarios, they might occur in a Markov chain Monte Carlo setting in which models are generated and perturbed randomly. Hence, in order to prevent modelling errors such as those described above from occurring during the rj-McMC inversion, after a number of trials we imposed a 20% limit on the velocity drop between any two consecutive layers of increasing depth (i.e., at every step of the Markov chain, the shear-velocity of layer k must be at least 80% of the shear-velocity of layer $k-1$ above it). This type of parametrisation was found to ensure that the models produced in the Markov chain did not exhibit the problems shown in Fig. 16(c) and (d), while still allowing velocity to decrease with depth if needed.

5.2 Shear-wave velocity maps

We performed transdimensional Love-wave group-velocity inversion at all possible geographical points in the East Irish Sea basin (black box in Fig. 15) by running 16 parallel Markov chains for 2 million iterations, discarding the first 5×10^5 samples on each chain as burn-in, and only retaining every 200$^{\text{th}}$ sample for analysis. In order to prevent the prior from biasing the final results, we used very wide priors and set their ranges to 0.5–8.5 km s^{-1} for v_S, 0–60 km for the depth of Voronoi nuclei, 2–30 for the number of layers, and 0.01–10.01 for γ.

Figure 17 shows the results of the Love-wave group-velocity inversion below the point -4°E, 54°N. The 2D posterior on v_S in Fig. 17(a) shows the presence of a clear peak in the shear-velocity posterior distribution corresponding to a profile of the maximum-probability v_S in panel 17(b), down to ~ 40 km. The average v_S profile in Fig. 17(b) displays a relatively sharp increase in velocity at 4–5 km depth, which is also marked by a peak in the posterior density

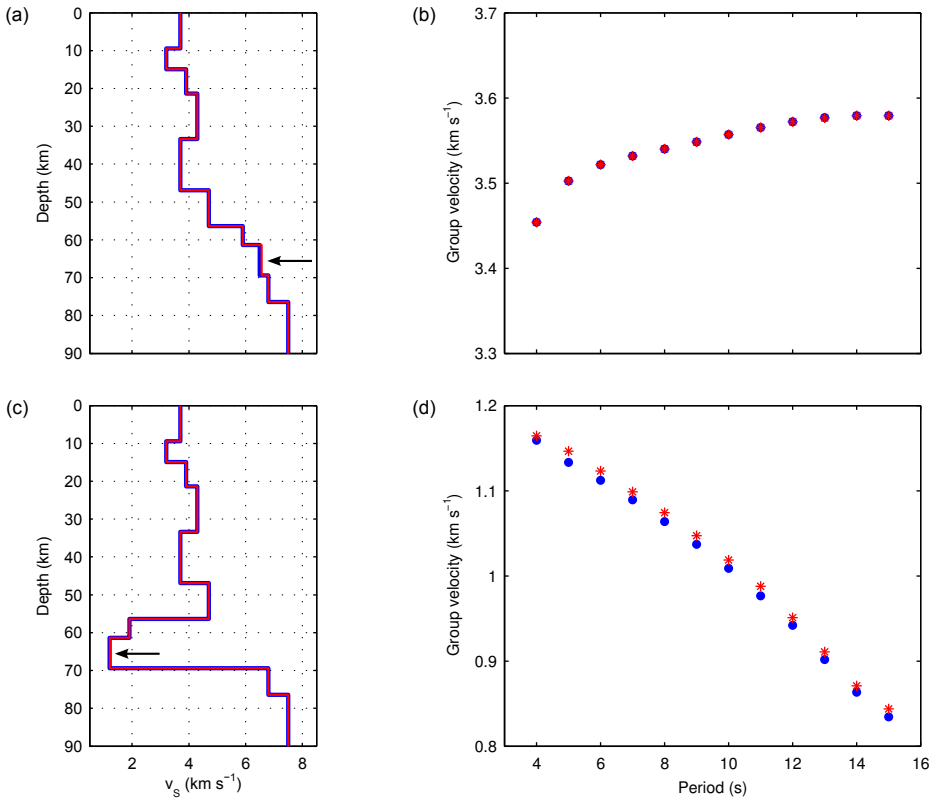

Figure 16. Example of Love-wave group-velocity dispersion modelling using DISPER80 on (a)-(b) a shear-velocity profile in which v_S generally increases with depth, and (c)-(d) an inverted shear-velocity profile which contains a low-velocity layer at large depths. The blue and red v_S profiles in (a) and (c) produce the dispersion curves denoted by the blue circles and red asterisks, respectively, in (b) and (d). The red profiles are obtained by increasing the shear-velocity of the layer near 65 km depth (indicated by the arrow) by 1% relative to the shear velocity of the same layer in the blue profiles.

of discontinuities in Fig. 17(c) and is likely to correspond to the depth of the sedimentary basin at this geographical location. As expected, the standard deviation profile in Fig. 17(b) shows an increase in uncertainty with depth, indicating that the depth limit of any significant resolution is around $\sim$ 25 km. The posterior on the number layers in Fig. 17(d) peaks at 2, indicating that simpler models are favoured during inversion. Finally, Fig. 17(f) shows the data that was inverted, and the best-fitting dispersion curve from each of the 16 Markov chains. As expected, the spread in the modelled curves depends on the size of the uncertainties, being the lowest where uncertainties are smallest (i.e., 12 and 15 seconds period). However, the posterior distribution on noise hyperparameter γ (Fig. 17(e)) presents a peak near 2, indicating that the uncertainties obtained from tomography might be too low to be consistent with these models and should be scaled up by a factor of ~ 2.

The average v_S and standard deviation maps in Fig 18 were obtained by performing

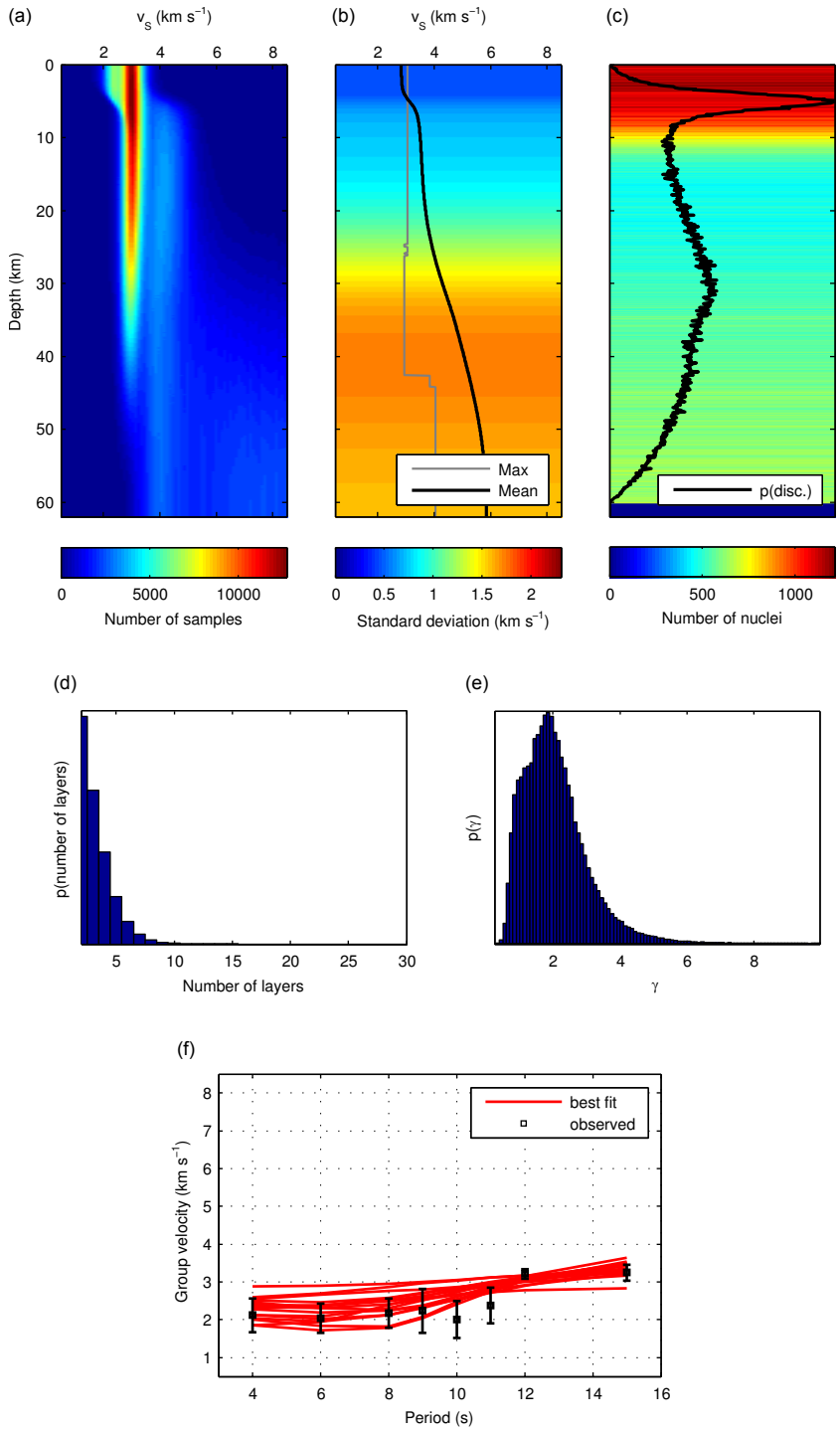

Figure 17. Results of Love-wave group-velocity inversion for shear velocity (v_S) structure with depth below −4°E, 54°N. (a) Posterior PDF on v_S as a function of depth. (b) Average v_S (black solid line), maximum-probability v_S (grey solid line), and standard deviation of v_S (background image). (c) Posterior PDF on the depth of discontinuities (black solid line) and location of Voronoi nuclei (background image). (d) Posterior PDF on number of layers. (e) Posterior PDF on noise hyperparameter γ. (f) Observed and modelled data: the black squares denote the dispersion data points obtained from the average group-velocity maps in Figs 12–13, with one standard deviation uncertainties marked by error bars; the red solid lines denote the data obtained from the best-fitting model from each of the 16 Markov chains run for the depth inversion.

transdimensional Love-wave group-velocity inversion beneath 2145 geographical points within the black box in Fig. 15, merging all 1D profiles into a 3D model, and taking horizontal slices of average shear-velocity and standard deviation at various constant depths. Similarly, the vertical sections in Fig. 19 were obtained by taking vertical slices of the 3D model along profiles of constant latitude (panel (a)) and longitude (panel (b)). The structure of the sedimentary basin with depth can clearly be seen in the average v_S maps and vertical sections: the shear-velocity in the basin increases from the surface to 4 km depth, and little trace of sediment remains below 6 km. However, since this is associated with an increase in uncertainty, the increase in shear-velocity with depth may not be as sharp as indicated by the average maps.

In particular, Figs 18 and 19 show that the lowest velocities in the basin (found down to ~ 5 km depth between approximately $-4°$E and $-3.5°$E, and 53.5°N and 54°N) are replaced by high-velocities below 5 km. This behaviour is particularly evident in Fig. 19, where the average shear velocity of the basement and its corresponding standard deviation appear to be higher when this underlies the sedimentary basin. A comparison between the posterior probability distribution obtained at two geographical points located outside and within the Irish Sea sedimentary basin is shown in Fig. 20. Outside the basin, the posterior PDF on v_S (Fig. 20(a)) is unimodal and peaks near 3.4 km s^{-1} down to approximately 40 km depth. The average curve (Fig. 20(b)) follows the maximum-probability profile down to ~ 15 km, and is then mainly influenced by the prior on v_S below this depth. However, the maximum-probability curve does not appear to be affected by the v_S prior until much greater depths; this is likely to be due to most samples having only 2–3 very thick layers, which causes the peak of the PDF to remain relatively uniform. The lack of clear discontinuities at this geographical location can also be observed in Fig. 20(c). Within the basin area, the posterior PDF on v_S (Fig. 20(d)) is multimodal both within the sedimentary layer (i.e., down to ~ 5 km depth as also shown in panel (f)) and in the basement. The presence of multiple peaks in the posterior PDF accounts for the differences that can be observed between the average and maximum-probability curves shown in Fig. 20(e). Although the presence of multiple peaks in the posterior PDF in panel (d) is likely to be an artefact, we are presently unsure about the exact mechanisms that give rise to these features, and our research on this topic is ongoing. In particular, these artefacts may be caused by either the inversion method we used, or by an erroneous interpretation of higher-mode or spurious cross-mode events in the interferometric Green's functions as fundamental Love-wave modes (Halliday & Curtis 2008; Poli et al. 2013), or by a combination of both factors. We have, however, also observed similar behaviours when performing v_S depth inversion at geographical points located in other UK sedimentary basins.

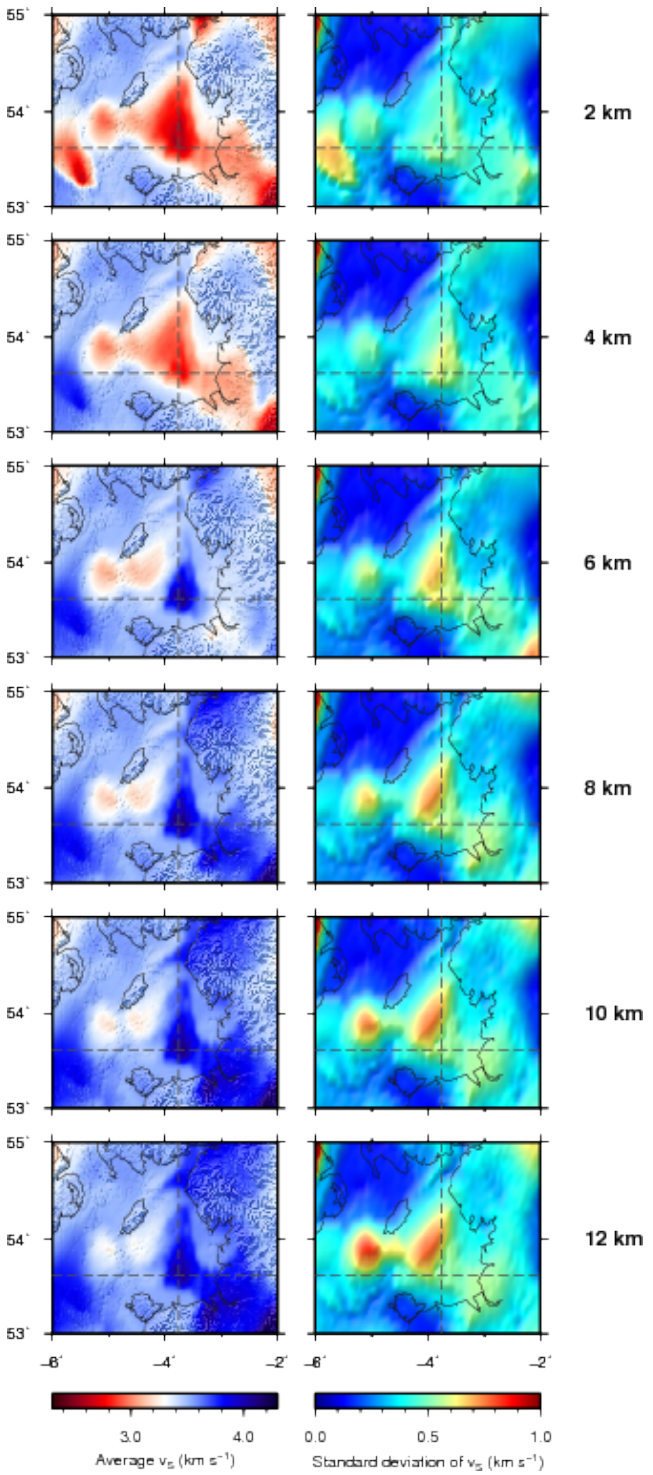

Figure 18. Results of Love-wave group-velocity inversion of 2145 dispersion curves in the East Irish Sea. Average (left) and standard deviation (right) maps of v_S between 2 and 12 km depth. The dashed grey lines denote the locations of the two vertical sections shown in Fig. 19.

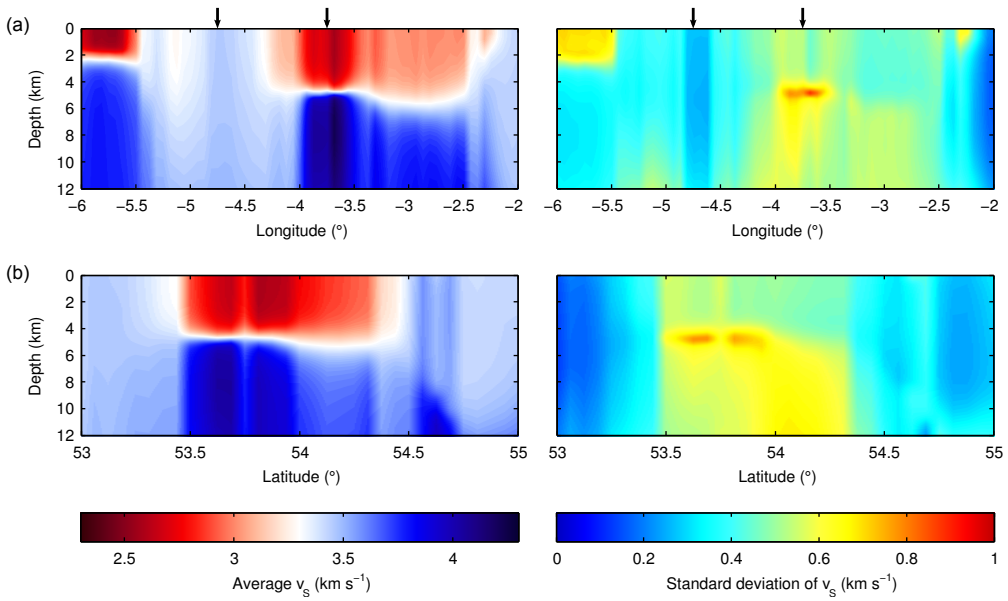

Figure 19. Vertical sections through the 3D crustal model of the East Irish Sea from Love-wave group-velocity inversion at (a) 53.625°N latitude and (b) −3.75°E longitude, showing average (left) and standard deviation (right) of v_S. The locations of the two sections are denoted by dashed grey lines in Fig. 18. The black arrows in panel (a) denote the locations of the two profiles shown in Fig. 20.

The relationship between the geological structures of the East Irish Sea basin and the results of depth inversion can be observed in Fig. 21. The Lagman and Eubonia Basins, containing up to 4 km of Carboniferous sediment (Quirk et al. 2006), can be identified by the low velocities to the south-east of the Isle of Man, while a high-velocity, north-east trending extension of the island known as the Ramsay-Whitehaven Ridge links the Isle of Man with the Lake District onshore. The Ramsay-Whitehaven Ridge is separated from the Lagman and Eubonia Basins by the Lagman, Eubonia and Shag Rock Faults, which run approximately NE-SW and can be identified by the sharp discontinuity in velocity running parallel to the south-eastern coast of the Isle of Man. The West Lancashire and Cheshire Basins can also be observed in the south-east sector of the maps as low-velocity zones down to approximately 4 km depth, which agrees with the known basin depths (Chadwick 1997; Mikkelsen & Floodpage 1997). The lowest velocity structure, located near −3.8°E, 53.7°N and reaching depths between approximately 4 and 6 km, corresponds to an area of rifting characterised by a large number of approximately N-S-striking normal faults.

Thus we have shown that the group velocity maps found in the first part of this work appear to be consistent with shear velocity structures that agree with previous studies, at least in terms of basin depths and overall geometry assuming that the latter is fault-bounded.

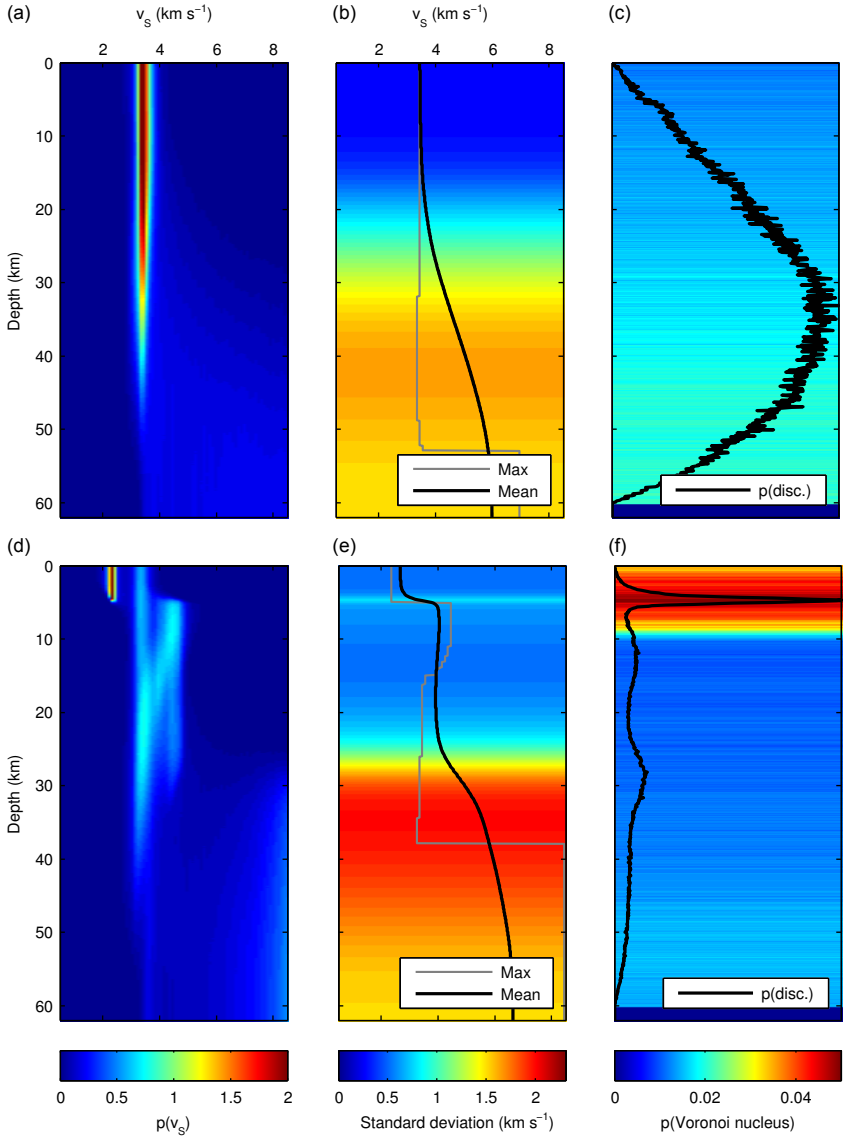

Figure 20. Results of Love-wave group-velocity inversion for shear velocity (v_S) structure with depth below −4.75°E, 53.625°N (top row), and −3.75°E, 53.625°N (bottom row). (a),(d) Posterior PDF on v_S as a function of depth. (b),(e) Average v_S (black solid line), maximum-probability v_S (grey solid line), and standard deviation of v_S (background image). (c),(f) Posterior PDF on the depth of discontinuities (black solid line) and location of Voronoi nuclei (background image). The geographical location of the two profiles is marked by black arrows in Fig. 19(a). Note that the colour scales in the left and right column are clipped.

In order to fit the mapped group velocities their uncertainties had to be increased by around a factor of 2. This indicates that either estimates were too low from the group-velocity tomography, or that the models used for depth inversion were too restrictive to fit the data. It is possible that freely varying P-velocity and density structures, or adding anisotropy to both

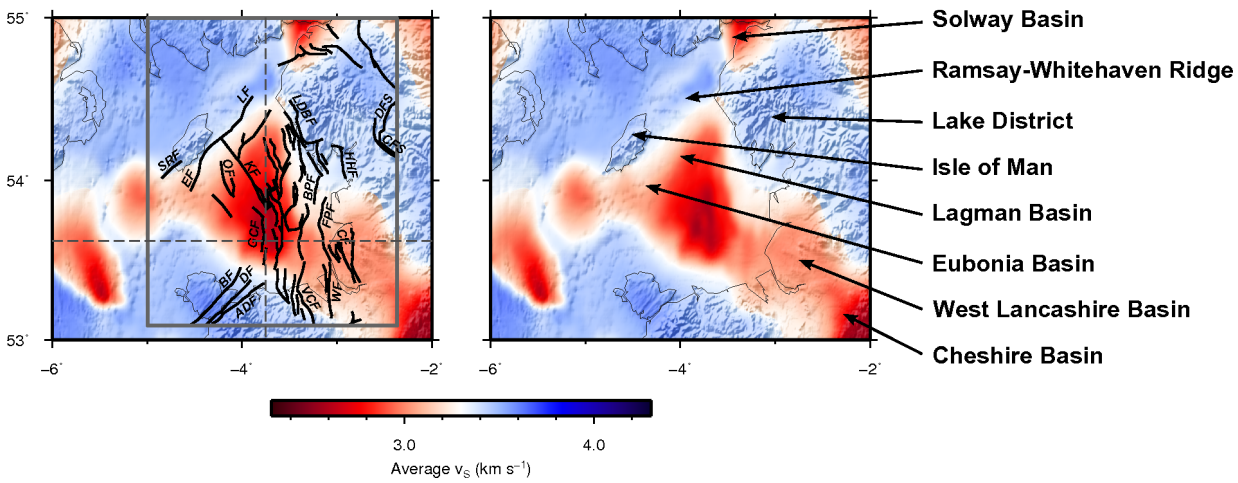

Figure 21. Average v_S map at 2 km depth from Love-wave group-velocity inversion and main structural elements in the East Irish Sea basin. Major faults are overlaid in the grey box on the left-hand map, and the main geological structures are indicated on the right-hand map. Faults are after Arter & Fagin (1993) and are abbreviated as follows: Lagman Fault (LF); Eubonia Fault (EF); Shag Rock Fault (SRF); Ogham Fault (OF); Keys Fault (KF); Godred Croven Fault (GCF); Berw Fault (BF); Dinorwic (DF); Aber-Dinnle Fault (ADF); Lake District Boundary Fault (LDBF); Blackpool Fault (BPF); Vale of Clwyd Fault (VCF); Humphrey Head Fault (HHF); Formby Point Fault (FPF); Croxteth Fault (CF); Woodchurch Fault (WF); Dent Faults (DFS); Craven Faults (CFS). The dashed grey lines on the left-hand map denote the locations of the two vertical sections shown in Fig. 19.

tomography and depth inversion, would have provided the freedom to fit the group velocities without this additional factor of 2, which might constitute the direction of valuable future research.

6 COMPUTATIONAL COST

The benefits of the algorithms used herein come at the price of a relatively high computational cost, which may limit the applicability of the method when sufficient computational power is not available. For instance, each of the tomographic inversions discussed in Section 4.3 was run over 16 independent Markov chains in parallel and took about one month of computation time, which was mainly spent in recalculating all raypaths at each Markov chain iteration. In their original approach, Bodin & Sambridge (2009) overcame this issue by fixing the ray geometry; however, as shown by Galetti et al. (2015) this may introduce artefacts and biases into the solution, hence the use of correct raypaths at each step of the Markov chain should not be overlooked. In fact, experimental parallelisation of the raytracing subroutine over sources has been shown to reduce computation time quite dramatically, making the use of this fully

non-linear tomography method more practical in cases where computing time is an issue or when much denser arrays of sources and receivers are available compared to those used in this paper. In addition, rather than using an equally-spaced grid in latitude and longitude, considerable savings in computation time may be made by adapting the size of the modelling grid to the geographical location of the inversion (i.e., at UK latitudes, one degree longitude is approximately half the length of one degree latitude). Similarly, the rj-McMC group velocity depth inversion step took 10–15 minutes per dispersion curve, which in this case limited the application of the second step of the method to a relatively small sector around the East Irish Sea sedimentary basin. Nevertheless, the successful application of both inversion methods demonstrates how fully non-linear inversion is now a possibility, eliminating the need for any linearised approximations to be made during the inversion. Future work may therefore include extending the tomographic inversion to further periods, and performing Love-wave group-velocity inversion at all possible geographical points to obtain a 3D model of the crust beneath the majority of the British Isles.

7 CONCLUSIONS

We present the first maps of Love-wave group-velocity across the British Isles, and the corresponding shear velocity structures beneath the East Irish Sea basin. Using inter-station traveltimes obtained from ambient-noise cross-correlations and a fully non-linear transdimensional tomography method, we first produced Love-wave group velocity maps within eight different frequency bands and maps of their associated uncertainties. These maps provide an insight into the crustal structure of the British Isles, and correctly identify a number of well known geological structures. Particularly, high velocities are observed in the Scottish Highlands, in the Southern Uplands, in the Pennines and around granitic intrusions in Wales and Cornwall, while low velocities are observed in a number of sedimentary basins such as those in the south of England, the Moray Firth, the Midland Valley and the East Irish Sea. A robust high-velocity feature is also observed in the East Midlands, and may be related to the presence of granitic batholiths and dykes in the subsurface. At greater depths sampled by the 12 and 15 seconds period maps, most sedimentary basins are no longer visible, hence maps in these frequency bands are likely to be mainly representative of basement rocks.

In a second stage, we created a set of one-dimensional dispersion curves over a regular grid of geographical points using information from the group velocity and standard deviation maps at different periods. We selected all valid dispersion curves corresponding to geographical points within an area spanning the East Irish Sea basin and independently inverted them

for the shear velocity structure with depth. Most of the resulting shear-velocity models are relatively simple and best described by two to three layers (probably due to the relatively limited spread of group velocity periods available), and show an approximate depth to basement of 5 km in this basin. By joining all of the one-dimensional profiles, we produced a 3D model of the crust beneath the East Irish Sea which clearly shows the sedimentary basin structure with depth.

Overall, the combination of fully non-linear rj-McMC tomography and Love-wave group-velocity inversion proved to be a practical two-step method to investigate the variation of shear-velocity with depth in the crust while keeping forward-modelling- and parametrisation-related biases to a minimum. Thanks to the Bayesian nature of both inversion steps, ensembles of hundreds of thousands of models, rather than single models, were produced at each inversion stage. In addition, the ability to estimate the number of parameters and the data noise level as part of the inversion process allowed the algorithm to dynamically adapt the model to the available information.

8 ACKNOWLEDGEMENTS

We thank M. Sambridge, T. Bodin and N. Rawlinson for help with the rj-McMC tomography and group velocity inversion codes, G. Meles for help with theoretical aspects of the work, and the Natural Environment Research Council and Schlumberger plc for support and for granting us permission to publish. We also thank M. Ritzwoller, N. Rawlinson and G. Jin for their constructive reviews which helped to improve this paper. Finally, we thank the BGS, RUSH-II, BISE, GEOFON and AWE Blacknest UKNet arrays, and the IRIS and ORFEUS data centres who provided the seismic noise data used in this study. Many of the figures in this paper were plotted using the Generic Mapping Tools (Wessel & Smith 1995). Random numbers within the rj-McMC tomography code were generated using the Mersenne Twister routine *genrand* by M. Matsumoto and T. Nishimura (Hiroshima University).

REFERENCES

Arrowsmith, S. J., Kendall, M., White, N., VanDecar, J. C., & Booth, D. C., 2005. Seismic imaging of a hot upwelling beneath the British Isles, *Geology*, **33**(5), 345–348.

Arter, G. & Fagin, S. W., 1993. The Fleetwood Dyke and the Tynwald fault zone, Block 113/27, East Irish Sea Basin, *Geological Society, London, Petroleum Geology Conference series*, **4**, 835–843.

Asencio, E., Knapp, J. H., Owens, T. J., & Helffrich, G., 2003. Mapping fine-scale heterogeneities

within the continental mantle lithosphere beneath Scotland: Combining active- and passive-source seismology, *Geology*, **31**(6), 477–480.

Baptie, B., 2010. Seismogenesis and state of stress in the UK, *Tectonophysics*, **482**(1–4), 150–159.

Bastow, I. D., Owens, T. J., Helffrich, G., & Knapp, J. H., 2007. Spatial and temporal constraints on sources of seismic anisotropy: Evidence from the Scottish highlands, *Geophysical Research Letters*, **34**(5), L05305.

Bensen, G. D., Ritzwoller, M. H., Barmin, M. P., Levshin, A. L., Lin, F., Moschetti, M. P., Shapiro, N. M., & Yang, Y., 2007. Processing seismic ambient noise data to obtain reliable broad-band surface wave dispersion measurements, *Geophysical Journal International*, **169**(3), 1239–1260.

Bensen, G. D., Ritzwoller, M. H., & Shapiro, N. M., 2008. Broadband ambient noise surface wave tomography across the United States, *Journal of Geophysical Research*, **113**(B5), B05306.

Bodin, T. & Sambridge, M., 2009. Seismic tomography with the reversible jump algorithm, *Geophysical Journal International*, **178**(3), 1411–1436.

Bodin, T., Sambridge, M., Rawlinson, N., & Arroucau, P., 2012a. Transdimensional tomography with unknown data noise, *Geophysical Journal International*, **189**(3), 1536–1556.

Bodin, T., Sambridge, M., Tkalčić, H., Arroucau, P., Gallagher, K., & Rawlinson, N., 2012b. Transdimensional inversion of receiver functions and surface wave dispersion, *Journal of Geophysical Research: Solid Earth*, **117**(B2), B02301.

British Geological Survey, 2015. BGS Earthquake Database Search, http://www.earthquakes.bgs.ac.uk/earthquakes/dataSearch.html, Online; last accessed: 30 July 2015.

Campillo, M. & Paul, A., 2003. Long-Range Correlations in the Diffuse Seismic Coda, *Science*, **299**(5606), 547–549.

Chadwick, R. & Pharaoh, T., 1998. The seismic reflection Moho beneath the United Kingdom and adjacent areas, *Tectonophysics*, **299**(4), 255–279.

Chadwick, R. A., 1997. Fault analysis of the Cheshire Basin, NW England, *Geological Society, London, Special Publications*, **124**(1), 297–313.

Cho, K. H., Herrmann, R. B., Ammon, C. J., & Lee, K., 2007. Imaging the Upper Crust of the Korean Peninsula by Surface-Wave Tomography, *Bulletin of the Seismological Society of America*, **97**(1B), 198–207.

Curtis, A., Trampert, J., Snieder, R., & Dost, B., 1998. Eurasian fundamental mode surface wave phase velocities and their relationship with tectonic structures, *Journal of Geophysical Research*, **103**(B11), 26919–26947.

Curtis, A., Gerstoft, P., Sato, H., Snieder, R., & Wapenaar, K., 2006. Seismic interferometry—turning noise into signal, *The Leading Edge*, **25**(9), 1082–1092.

de Ridder, S. & Dellinger, J., 2011. Ambient seismic noise eikonal tomography for near-surface imaging at Valhall, *The Leading Edge*, **30**(5), 506–512.

de Ridder, S. A. L., Biondi, B. L., & Clapp, R. G., 2014. Time-lapse seismic noise correlation tomography at Valhall, *Geophysical Research Letters*, **41**(17), 6116–6122.

Dentith, M. C. & Hall, J., 1989. MAVIS – an upper crustal seismic refraction experiment in the Midland Valley of Scotland, *Geophysical Journal International*, **99**(3), 627–643.

Dentith, M. C. & Hall, J., 1990. MAVIS: Geophysical constraints on the structure of the Carboniferous basin of West Lothian, Scotland, *Earth and Environmental Science Transactions of the Royal Society of Edinburgh*, **81**, 117–126.

Galetti, E. & Curtis, A., 2012. Generalised receiver functions and seismic interferometry, *Tectonophysics*, **532–535**, 1–26.

Galetti, E., Curtis, A., Meles, G. A., & Baptie, B., 2015. Uncertainty loops in travel-time tomography from nonlinear wave physics, *Physical Review Letters*, **114**(14), 148501.

Gallagher, K., Bodin, T., Sambridge, M., Weiss, D., Kylander, M., & Large, D., 2011. Inference of abrupt changes in noisy geochemical records using transdimensional changepoint models, *Earth and Planetary Science Letters*, **311**, 182–194.

Halliday, D. & Curtis, A., 2008. Seismic interferometry, surface waves and source distribution, *Geophysical Journal International*, **175**(3), 1067–1087.

Haney, M. M. & Douma, H., 2010. Imaging lateral heterogeneity at Coronation Field with surface waves, *SEG Technical Program Expanded Abstracts 2010*, pp. 1851–1855.

Haney, M. M. & Douma, H., 2012. Rayleigh-wave tomography at Coronation Field, Canada: The topography effect, *The Leading Edge*, **31**(1), 54–61.

Herrmann, R. B. & Ammon, C. J., 2002. *Computer Programs in Seismology - Surface Waves, Receiver Functions and Crustal Structure*.

Jay, J., Pritchard, M., West, M., Christensen, D., Haney, M., Minaya, E., Sunagua, M., McNutt, S., & Zabala, M., 2012. Shallow seismicity, triggered seismicity, and ambient noise tomography at the long-dormant Uturuncu Volcano, Bolivia, *Bulletin of Volcanology*, **74**, 817–837.

Kurita, T., 1973. Regional variations in the structure of the crust in the central United States from P-wave spectra, *Bulletin of the Seismological Society of America*, **63**(5), 1663–1687.

Li, H., Bernardi, F., & Michelini, A., 2010a. Love wave tomography in Italy from seismic ambient noise, *Earthquake Science*, **23**(5), 487–495.

Li, H., Su, W., Wang, C.-Y., Huang, Z., & Lv, Z., 2010b. Ambient noise Love wave tomography in the eastern margin of the Tibetan plateau, *Tectonophysics*, **491**(1–4), 194–204.

Lin, F.-C. & Ritzwoller, M. H., 2011. Helmholtz surface wave tomography for isotropic and azimuthally anisotropic structure, *Geophysical Journal International*, **186**(3), 1104–1120.

Lin, F.-C., Ritzwoller, M. H., Townend, J., Bannister, S., & Savage, M. K., 2007. Ambient noise Rayleigh wave tomography of New Zealand, *Geophysical Journal International*, **170**(2), 649–666.

Lin, F.-C., Moschetti, M. P., & Ritzwoller, M. H., 2008. Surface wave tomography of the western United States from ambient seismic noise: Rayleigh and Love wave phase velocity maps, *Geophysical*

Journal International, **173**(1), 281–298.

Luckett, R. & Baptie, B., 2015. Local earthquake tomography of Scotland, *Geophysical Journal International*, **200**(3), 1538–1554.

Masterlark, T., Haney, M., Dickinson, H., Fournier, T., & Searcy, C., 2010. Rheologic and structural controls on the deformation of Okmok volcano, Alaska: FEMs, InSAR, and ambient noise tomography, *Journal of Geophysical Research*, **115**(B2), B02409.

Mikkelsen, P. W. & Floodpage, J. B., 1997. The hydrocarbon potential of the Cheshire Basin, *Geological Society, London, Special Publications*, **124**(1), 161–183.

Mordret, A., Landès, M., Shapiro, N. M., Singh, S. C., Roux, P., & Barkved, O. I., 2013a. Near-surface study at the Valhall oil field from ambient noise surface wave tomography, *Geophysical Journal International*, pp. 1–17.

Mordret, A., Shapiro, N. M., Singh, S. S., Roux, P., & Barkved, O. I., 2013b. Helmholtz tomography of ambient noise surface wave data to estimate Scholte wave phase velocity at Valhall Life of the Field, *Geophysics*, **78**(2), WA99–WA109.

Nagaoka, Y., Nishida, K., Aoki, Y., Takeo, M., & Ohminato, T., 2012. Seismic imaging of magma chamber beneath an active volcano, *Earth and Planetary Science Letters*, **333–334**(0), 1–8.

Nicolson, H., Curtis, A., Baptie, B., & Galetti, E., 2012. Seismic interferometry and ambient noise tomography in the British Isles, *Proceedings of the Geologists' Association*, **123**(1), 74–86.

Nicolson, H., Curtis, A., & Baptie, B., 2014. Rayleigh Wave Tomography of the British Isles from Ambient Seismic Noise, *Geophysical Journal International*, **198**(2), 637–655.

Picozzi, M., Parolai, S., Bindi, D., & Strollo, A., 2009. Characterization of shallow geology by high-frequency seismic noise tomography, *Geophysical Journal International*, **176**(1), 164–174.

Pilz, M., Parolai, S., Picozzi, M., & Bindi, D., 2012. Three-dimensional shear wave velocity imaging by ambient seismic noise tomography, *Geophysical Journal International*, **189**(1), 501–512.

Poli, P., Pedersen, H. A., Campillo;, M., & the POLENET/LAPNET Working Group, 2013. Noise directivity and group velocity tomography in a region with small velocity contrasts: the northern Baltic shield, *Geophysical Journal International*, **192**(1), 413–424.

Quirk, D., Burnett, D., & Thomas, G., 2006. The Castletown Limestone, in *A New History of the Isle of Man: The Evolution of the Natural Landscape*, vol. 1, chap. 5, pp. 90–111, eds Chiverrell, R. & Thomas, G., Liverpool University Press.

Rawlinson, N. & Sambridge, M., 2004. Wave front evolution in strongly heterogeneous layered media using the fast marching method, *Geophysical Journal International*, **156**(3), 631–647.

Rawlinson, N. & Sambridge, M., 2005. The fast marching method: an effective tool for tomographic imaging and tracking multiple phases in complex layered media, *Exploration Geophysics*, **36**(4), 341–350.

Rawlinson, N., Pozgay, S., & Fishwick, S., 2010. Seismic tomography: A window into deep Earth, *Physics of the Earth and Planetary Interiors*, **178**(3–4), 101–135.

Ray, A., Key, K., Bodin, T., Myer, D., & Constable, S., 2014. Bayesian inversion of marine CSEM data from the Scarborough gas field using a transdimensional 2-D parametrization, *Geophysical Journal International*, **199**(3), 1847–1860.

Roux, P., 2009. Passive seismic imaging with directive ambient noise: application to surface waves and the San Andreas Fault in Parkfield, CA, *Geophysical Journal International*, **179**(1), 367–373.

Sabra, K. G., Gerstoft, P., Roux, P., Kuperman, W. A., & Fehler, M. C., 2005. Surface wave tomography from microseisms in Southern California, *Geophysical Research Letters*, **32**(14), L14311.

Saito, M., 1988. DISPER80: A Subroutine Package for the Calculations of Seismic Normal-Mode Solutions, in *Seismological Algorithms – Computational Mehtods and Computer Programs*, chap. 4.1, pp. 293–319, ed. Doornbos, D. J., Academic Press.

Saygin, E. & Kennett, B. L. N., 2010. Ambient seismic noise tomography of Australian continent, *Tectonophysics*, **481**(1–4), 116–125.

Schimmel, M. & Paulssen, H., 1997. Noise reduction and detection of weak, coherent signals through phase-weighted stacks, *Geophysical Journal International*, **130**(2), 497–505.

Schimmel, M., Stutzmann, E., & Gallart, J., 2011. Using instantaneous phase coherence for signal extraction from ambient noise data at a local to a global scale, *Geophysical Journal International*, **184**(1), 494–506.

Schuster, G. T., 2009. *Seismic Interferometry*, Cambridge University Press.

Shapiro, N. M., Campillo, M., Stehly, L., & Ritzwoller, M. H., 2005. High-Resolution Surface-Wave Tomography from Ambient Seismic Noise, *Science*, **307**(5715), 1615–1618.

Snieder, R., 2004. Extracting the Green's function from the correlation of coda waves: A derivation based on stationary phase, *Physical Review E*, **69**(4), 046610.

Tomlinson, J. P., Denton, P., Maguire, P. K. H., & Booth, D. C., 2006. Analysis of the crustal velocity structure of the British Isles using teleseismic receiver functions, *Geophysical Journal International*, **167**(1), 223–237.

van Manen, D.-J., Robertsson, J. O. A., & Curtis, A., 2005. Modeling of Wave Propagation in Inhomogeneous Media, *Physical Review Letters*, **94**(16), 164301.

van Manen, D.-J., Curtis, A., & Robertsson, J. O. A., 2006. Interferometric modeling of wave propagation in inhomogeneous elastic media using time reversal and reciprocity, *Geophysics*, **71**(4), SI47–SI60.

Wapenaar, K., 2004. Retrieving the Elastodynamic Green's Function of an Arbitrary Inhomogeneous Medium by Cross Correlation, *Physical Review Letters*, **93**(25), 254301.

Wapenaar, K. & Fokkema, J., 2006. Green's function representations for seismic interferometry, *Geophysics*, **71**(4), SI33–SI46.

Wapenaar, K., Draganov, D., Snieder, R., Campman, X., & Verdel, A., 2010a. Tutorial on seismic interferometry: Part 1 – Basic principles and applications, *Geophysics*, **75**(5), 75A195–75A209.

Wapenaar, K., Slob, E., Snieder, R., & Curtis, A., 2010b. Tutorial on seismic interferometry: Part 2

– Underlying theory and new advances, *Geophysics*, **75**(5), 75A211–75A227.

Wessel, P. & Smith, W., 1995. New version of the Generic Mapping Tools released, *Eos, Transactions American Geophysical Union*, **76**(33), 329.

Woodcock, N. H. & Strachan, R., 2012. *Geological History of Britain and Ireland*, Wiley-Blackwell, 2nd edn.

Yang, Y., Ritzwoller, M. H., Levshin, A. L., & Shapiro, N. M., 2007. Ambient noise Rayleigh wave tomography across Europe, *Geophysical Journal International*, **168**(1), 259–274.

Young, M., Rawlinson, N., & Bodin, T., 2013. Transdimensional inversion of ambient seismic noise for 3D shear velocity structure of the Tasmanian crust, *Geophysics*, **78**(3), WB49–WB62.